PAPER

Kinetic electron model for plasma thruster plumes

IOP Publishing Plasma Sources Science and Technology
Plasma Sources Sci. Technol. **27** (2018) 035013 (18pp) https://doi.org/10.1088/1361-6595/aab3a1

Kinetic electron model for plasma thruster plumes

Mario Merino, Javier Mauriño and Eduardo Ahedo

Equipo de Propulsión Espacial y Plasmas (EP2), Universidad Carlos III de Madrid, Leganés, Spain

E-mail: mario.merino@uc3m.es

Received 23 December 2017, revised 9 February 2018
Accepted for publication 2 March 2018
Published 28 March 2018

Abstract

A paraxial model of an unmagnetized, collisionless plasma plume expanding into vacuum is presented. Electrons are treated kinetically, relying on the adiabatic invariance of their radial action integral for the integration of Vlasov's equation, whereas ions are treated as a cold species. The quasi-2D plasma density, self-consistent electric potential, and electron pressure, temperature, and heat fluxes are analyzed. In particular, the model yields the collisionless cooling of electrons, which differs from the Boltzmann relation and the simple polytropic laws usually employed in fluid and hybrid PIC/fluid plume codes.

Keywords: electric propulsion, plasma thrusters, plasma plumes, kinetic models, collisionless plasma, electron cooling

1. Introduction

The operation of electric space propulsion systems such as gridded ion thrusters (GITs) and Hall effect thrusters (HETs) results in the directed expansion of a plasma jet into vacuum, consisting of hypersonic ions with velocities of the order of tens of km s^{-1} and thermal electrons with temperatures of a few eV. These plasma plumes can interact mechanically, chemically, and electrically with nearby objects, potentially damaging or contaminating their surfaces [1–4]. This affects in particular the solar arrays of the spacecraft that carries the electric thruster. The dense emitted plasma also dominates the spacecraft electric charging process, over the effect of the more tenuous environmental plasma and the photoelectric effect on sunlit surfaces [5, 6]. Consequently, electric propulsion plasma plumes play an important role in space system engineering and constitute a serious concern for satellite integrators. Plasma beams expanding into vacuum are also transversal to many different fields, such as plasma material processing [7, 8] and astrophysics [9].

Plasma thruster plumes have been extensively researched in the laboratory [10–18] and in space [19–23]. Existing experimental data show the monotonic decrease of plasma density, electron temperature and electric potential along the expansion. In the near-region, which extends for the first few thruster radii outside of the thruster, residual electric and magnetic fields from the thruster, collisions with the larger concentration of neutrals there, and three-dimensional non-homogeneities resulting from the geometry of the thruster and its neutralizer, exert an important influence on the plasma dynamics [12, 13, 24, 25]. Downstream, in the far-region, these effects become negligible, the inhomogeneities in the radial density profile smooth out, and the plasma is near-collisionless, unmagnetized, and quasineutral [11, 16, 26, 27].

Together with these experimental observations, the present understanding of plasma plumes results from several models. Full particle-in-cell (PIC) approaches have been used to study the kinetic expansion of rarefied plasmas with mixed success; while this method yields great physical detail, the large extent of the plume domain and the reduced time scale of electron motion make them computationally hardly affordable, and thus impractical except for some specialized studies [28–30]. Moreover, the expansion causes the number of numerical macroparticles per cell to decrease downstream, resulting in high statistical noise and PIC regularization problems. Multi-fluid models, on the other hand, enable the quick estimation of the plasma properties in the plume [27, 31, 32], but have limited accuracy when dealing with a near-collisionless medium that can be far from local thermodynamic equilibrium, as they require external closure relations to truncate the infinite series of fluid equations, and do not provide the kinetic plasma response. Hybrid PIC/fluid models, which treat the heavy species as particles and the electrons as a fluid, combine some of the advantages of each

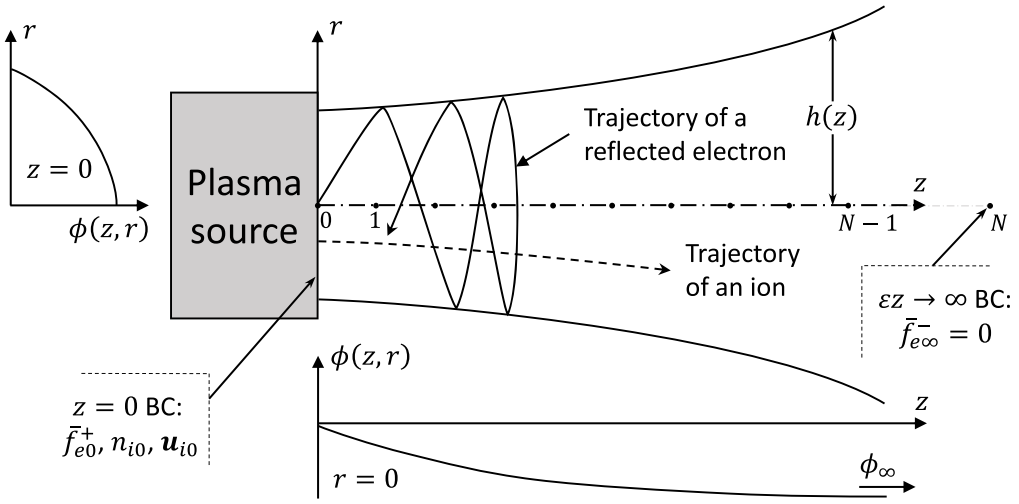

Figure 1. Sketch of the plasma plume expansion from an initial plane $z = 0$ (the upstream model boundary) to $z \to \infty$ (downstream boundary). The electric potential ϕ decreases gently in the axial direction to an asymptotic value ϕ_∞, and faster in the radial direction. Typical ion and electron trajectories are shown. The outer solid lines represent the characteristic radius of the plume at each z position, $h(z)$. The N dots on the plume axis represent the evaluation nodes used in the model of section 3.

approach [33–39]. This third way to study plasma plumes has thus become a popular alternative over the last few decades, during which multiple hybrid codes have been developed.

The need of a closure relation for the electron fluid affects both multi-fluid and hybrid models, and is one of their major downsides. Such closure is commonly applied at the pressure-tensor level, although approaches at the heat flux level also exist [1, 40]. The most basic but extended model relies on Boltzmann's relation, which results in isotropic, isothermal electrons [36, 40]. Unfortunately, while Boltzmann's relation is adequate for a confined electron population, and thus it is a valid approximation in the first part of the expansion, it predicts an infinite electric potential fall along the plume. A small improvement over that closure is to treat the electrons as a polytropic species [15, 27, 31, 41], which cools down at a rate given by the cooling exponent $\gamma > 1$, i.e. $T_e \propto n_e^{\gamma-1}$. While this model yields a finite electric potential fall, and can to some extent recover the electron temperature drop with the expansion, the self-consistent determination of this new parameter remains an open problem. Clearly, only a kinetic electron model can provide the satisfactory closure relation for a near-collisionless electron fluid model.

This article presents a quasi-2D kinetic model of a plasma plume and uses it to characterize several features of the electron expansion. The model assumes a collisionless, unmagnetized, quasineutral, steady-state plasma, providing a good description of the plume far-region. The integration of the electron model relies on the first-order conservation of an averaged action integral of motion, which is an adiabatic invariant under the assumption of a small plume divergence angle. The action integral plays an analogous role to the magnetic moment in the magnetized plasma expansion in a magnetic nozzle [42–45], and it was used successfully to describe the flow of unmagnetized ions in a convergent magnetic field by Martínez-Sánchez and Ahedo [46].

The electron velocity distribution function and its moments are computed, with a focus on the collisionless cooling of electrons. The results of this study can inform multi-fluid and hybrid codes, thus filling in the existing theoretical gap on the electron closure. As an example, an approximated, 'lumped' polytropic model that respects the total potential fall of the kinetic solution and depends on the plasma properties at emission is finally proposed, which can be easily implemented in existing numerical codes.

The rest of the paper is structured as follows. Section 2 introduces the general kinetic plasma plume model. This sets up a framework for solving the plasma expansion, which is particularized in section 3 for the case of a plasma plume with a radially-parabolic electric potential and semi-Maxwellian electrons upstream. Section 4 presents the numerical results of the plasma expansion. Then, in section 5, the simplified electron model based on a polytropic cooling law is proposed. Finally, section 6 presents some additional comments on the kinetic model in the light of the obtained results, including a discussion of its limits of validity, and section 7 gathers the main conclusions. A preliminary version of this work was presented in [47].

2. General kinetic model

The kinetic model of a plasma plume expanding into vacuum from $z = 0$, as sketched in figure 1, consists of the electron ('e') and ion ('i') submodels described below, which are used iteratively to find the self-consistent electric potential response. The plume is assumed to be steady-state, axisymmetric, non-rotating, quasineutral, collisionless and unmagnetized. These conditions are well satisfied in the plume far-region of common thrusters like GITs and HETs, i.e. downstream of the near-region where collisions with neutrals, thruster electromagnetic fields, and 3D features existing around the thruster become negligible, as described in the introduction.

The electric potential in a plasma plume decreases axially and radially, accelerating all ions downstream and confining

most of the electrons, as sketched in figure 1. In this model, the electric potential is assumed to confine all electrons radially, while only the most energetic electrons overcome the axial potential fall and escape downstream, to offset the ion current and produce a current-free plume.

The plume expansion is required to be paraxial, i.e. slowly diverging. In other words, the axial derivative of the self-consistent electric potential $\phi = \phi(z, r)$ needs to be of order $\varepsilon \ll 1$,

$$\frac{\partial \phi}{\partial z} = O(\varepsilon). \tag{1}$$

In contrast, the radial derivative $\partial\phi/\partial r$ is zeroth order. Under these assumptions, electrons typically perform many radial and azimuthal orbits before experiencing an important axial change of the electric potential.

2.1. Electron model

The Hamiltonian $H = H(z, r, \theta, p_z, p_r, p_\theta)$ of an electron in a steady-state, axisymmetric electric potential can be written as:

$$H = \frac{1}{2m_\mathrm{e}}\left(p_z^2 + p_r^2 + \frac{p_\theta^2}{r^2}\right) - e\phi(z, r), \tag{2}$$

with $p_z = m_\mathrm{e} v_z$, $p_r = m_\mathrm{e} v_r$, and $p_\theta = r m_\mathrm{e} v_\theta$. The mechanical energy $E = H$ and the canonical azimuthal momentum p_θ of the electron are conserved quantities of motion.

For $\varepsilon = 0$ (i.e. a zero-divergence plume), the potential is a function of r only, so the Hamiltonian has no dependency on z, and p_z is invariant. The perpendicular and axial energies are then independently conserved quantities:

$$E_\perp = \frac{1}{2m_\mathrm{e}}\left(p_r^2 + \frac{p_\theta}{r^2}\right) - e\phi(r), \tag{3}$$

$$E_z = E - E_\perp. \tag{4}$$

The radially-trapped electrons bounce back and forth between certain limit values r_- and r_+ while moving in the z and θ directions. The radial action integral can be defined along one such radial orbit:

$$J_r = \oint p_r \mathrm{d}r, \tag{5}$$

and is another conserved quantity of motion. The conjugated Hamilton–Jacobi phase-angle variable [48] that parametrizes the radial motion is

$$\beta_r = \frac{\partial}{\partial J_r}\int p_r \mathrm{d}r = m_\mathrm{e}\frac{\partial H}{\partial J_r}\int \frac{\mathrm{d}r}{p_r}. \tag{6}$$

The variable β_r grows linearly with time and increases by one unit every full radial orbit, with $\dot{\beta}_r = \partial H/\partial J_r$. Finally, under these conditions, it is possible to write the Hamiltonian as a function of p_z, J_r, and p_θ only. The conservation of J_r holds exactly also for separable electric potentials of the form $\phi(z, r) = \phi_z(z) + \phi_r(r)$.

For $0 < \varepsilon \ll 1$ and a non-separable potential $\phi(z, r)$, which is the case of interest in a plasma plume, E_z and $E_\perp$ are not independently conserved, and electron energy can indeed flow between the perpendicular directions of motion (r, θ) and the axial one (z). The definitions of J_r and β_r of equations (5) and (6) may nevertheless still be used, by treating z, p_z as constants inside the integrals. Now, however, J_r varies in time, with

$$\dot{J}_r = e\left(\oint \frac{\partial \phi}{\partial z}\frac{p_z}{p_r}\mathrm{d}r - \frac{\partial \phi}{\partial z}\oint \frac{p_z}{p_r}\mathrm{d}r\right). \tag{7}$$

Likewise, β_r no longer increases linearly in time:

$$\dot{\beta}_r = \frac{\partial H}{\partial J_r}\left[1 - em_\mathrm{e}\left(\int \frac{\partial \phi}{\partial z}\frac{p_z}{p_r^3}\mathrm{d}r + \frac{\partial \phi}{\partial z}\int \frac{p_z}{p_r^3}\mathrm{d}r\right)\right]. \tag{8}$$

Additionally, the relation between E and p_z, J_r, and p_θ codified in the Hamiltonian now also has a dependency on z at order ε,

$$E = E(z, p_z, J_r, p_\theta). \tag{9}$$

Notwithstanding this, action integrals like J_r are *adiabatic invariants* under small perturbations [48]. This means that, while J_r can have *periodic* variations of order ε, its *secular* changes are only of order ε^2 or higher, as can be shown by detailed inspection of the time integral of equation (7). Likewise, $\dot{\beta}_r$ in equation (8) has only periodic variations to order ε. The conservation of E, p_θ, and the adiabatic invariance of J_r can be exploited to simplify the solution of the electron kinetic equation. The electron velocity distribution function f_e is decomposed into a β_r-averaged value $\bar{f}_\mathrm{e}$ plus an oscillation $\hat{f}_\mathrm{e}$ about this average:

$$f_\mathrm{e} = \bar{f}_\mathrm{e}(z, E, J_r, p_\theta) + \hat{f}_\mathrm{e}(z, \beta_r, E, J_r, p_\theta), \tag{10}$$

with $\bar{f}_\mathrm{e} = \int_0^1 f_\mathrm{e}\,\mathrm{d}\beta_r$ and $\int_0^1 \hat{f}_\mathrm{e}\,\mathrm{d}\beta_r = 0$. Since the chosen variables do not discriminate between electrons with positive or negative axial velocity, whenever this distinction is necessary, $\bar{f}_\mathrm{e}$ and $\hat{f}_\mathrm{e}$ are further split as $\bar{f}_\mathrm{e} = \bar{f}_\mathrm{e}^{+} + \bar{f}_\mathrm{e}^{-}$, $\hat{f}_\mathrm{e} = \hat{f}_\mathrm{e}^{+} + \hat{f}_\mathrm{e}^{-}$, where superscript '+' indicates $v_z \geqslant 0$, and '−,' $v_z < 0$.

The complete electron Vlasov equation for electrons then reads:

$$v_z\frac{\partial f_\mathrm{e}}{\partial z} + \dot{\beta}_r\frac{\partial \hat{f}_\mathrm{e}}{\partial \beta_r} + \dot{J}_r\frac{\partial f_\mathrm{e}}{\partial J_r} = 0. \tag{11}$$

Integration of this equation requires boundary conditions $\bar{f}_{\mathrm{e}0}^{+}(E, J_r, p_\theta)$ and $\hat{f}_{\mathrm{e}0}^{+}(\beta_r, E, J_r, p_\theta)$ at $z = 0$, which we refer to as upstream or *source electrons*, as well as $\bar{f}_{\mathrm{e}\infty}^{-}(E, J_r, p_\theta)$ and $\hat{f}_{\mathrm{e}\infty}^{-}(\beta_r, E, J_r, p_\theta)$ at $z \to \infty$, i.e. downstream or *background electrons*. For a plasma plume expanding into vacuum, there are no background electrons, i.e. $\bar{f}_{\mathrm{e}\infty}^{-}, \hat{f}_{\mathrm{e}\infty}^{-} = 0$.

Actual plasma sources are expected to deliver an electron population that is near-homogeneous in β_r, so that $\hat{f}_{\mathrm{e}0}^{+} = O(\varepsilon)$; in particular, for initially semi-Maxwellian electrons, $\hat{f}_{\mathrm{e}0}^{+}$ is strictly 0. If $\hat{f}_{\mathrm{e}0}^{+}$ is of order ε, then $\hat{f}_\mathrm{e}$ is also of order ε inside the plasma plume domain. Hence, we can establish the following ordering in the plasma plume,

$$\bar{f}_\mathrm{e} = O(1); \quad \hat{f}_\mathrm{e} = O(\varepsilon). \tag{12}$$

Then, after averaging over β_r, equation (11) becomes

$$v_z\frac{\partial \bar{f}_\mathrm{e}}{\partial z} = O(\varepsilon^2). \tag{13}$$

This means that, up to order ε, $\bar{f}_e$ is constant along z for each combination of E, J_r, p_θ, in regions delimited by the axial turning-point manifold $v_z = 0$, whose expression must be obtained by inversion of equation (9):

$$p_z(z, E, J_r, p_\theta) = m_e v_z = 0. \tag{14}$$

The region of phase space beyond this manifold is energetically forbidden.

In general, equation (14) has a non-monotonic behavior in the z direction, which results from two competing effects on the electron motion: on the one hand, the axially-decreasing electric potential causes a confining force that pushes electrons upstream. On the other hand, in the expanding electric potential, the adiabatic invariance of J_r and the conservation of p_θ create a net axial force on the radially-averaged electron motion that pushes them downstream. This second phenomenon is analogous to the magnetic mirror effect in a magnetized plasma, which pushes electrons in the direction of the expanding magnetic field due to the invariance of the magnetic moment of the electron. Consequently, the turning-point manifold can divide the solution existence domain into regions of four different types, or equivalently, the electrons into four subpopulations, according to their connectivity with the upstream and downstream boundaries. In the following, a subindex in parenthesis is used to denote an electron subpopulation.

1. Regions that connect with both the upstream and downstream boundaries. In these regions, electrons have enough energy to overcome all potential barriers and reach the opposite boundary without any reflection, and they are therefore termed *free electrons*. Hence, $\bar{f}^+_{e(1)} = \bar{f}^+_{e0}, \bar{f}^-_{e(1)} = \bar{f}^-_{e\infty} = 0$ in the free electron regions for an expansion into vacuum.
2. Electrons in regions connected only with the upstream boundary eventually turn back and return to the plasma source. They are called *reflected electrons*. In these regions, $\bar{f}^+_{e(2)} = \bar{f}^-_{e(2)} = \bar{f}^+_{e0}$.
3. Similarly, there are regions only connected with the downstream boundary. Therefore, for a plasma plume expanding into vacuum $\bar{f}^+_{e(3)} = \bar{f}^-_{e(3)} = \bar{f}^-_{e\infty} \equiv 0$, and these are *empty regions*.
4. Lastly, existence regions that are not connected with either the upstream or downstream boundaries may contain *doubly-trapped* electrons. Here, $\bar{f}^+_{e(4)} = \bar{f}^-_{e(4)}$, but the value of the distribution function remains otherwise undetermined, and the solution requires additional information from outside of the present kinetic model. As discussed in section 6, physical reasoning suggests that these regions must be populated by a f_e that is near-Maxwellian and near-continuous with neighboring parts of phase space.

To obtain the β_r-dependent part of the distribution function, $\hat{f}_e$, to comparable accuracy, it is necessary to tackle the rest of the non-averaged Vlasov equation (11) up to order ε, i.e.

$$v_z \frac{\partial \hat{f}_e}{\partial z} + \frac{\partial H}{\partial J_r}\frac{\partial \hat{f}_e}{\partial \beta_r} = -\dot{J}_r \frac{\partial \bar{f}_e}{\partial J_r} + O(\varepsilon^2). \tag{15}$$

This correction to f_e is not computed in the present work. As a result, the obtained solution $f_e = \bar{f}_e$ is strictly only accurate to zeroth order in ε. Once $\bar{f}_e$ is known, any moment of the electron species, or of a particular electron subpopulation, can be computed as described in the appendix.

2.2. Ion model

The ions emitted by a plasma thruster are commonly much colder than the electron population, $T_i \ll T_e$. Additionally, ions are hypersonic [27], with a bulk velocity $\boldsymbol{u}_i$ about 5–40 times larger than the plasma sonic velocity $c_s = \sqrt{T_e/m_i}$. Nonetheless, except for the lightest propellants, $\boldsymbol{u}_i$ is still much less than the electron thermal velocity, $c_e = \sqrt{T_e/m_e}$. Thus, the following ordering of velocities is satisfied in a plasma thruster plume:

$$c_i \ll c_s \ll u_i \ll c_e. \tag{16}$$

Moreover, ions are accelerated downstream by the electric field in the plasma plume, so all of them are *free ions* that undergo no axial reflections. Consequently, their motion is far simpler than that of electrons.

Neglecting the dispersion in the ion velocity distribution function, ions are modeled as a cold species that satisfies the following steady-state continuity and momentum fluid equations,

$$\nabla \cdot (n_i \boldsymbol{u}_i) = 0, \tag{17}$$

$$m_i(\boldsymbol{u}_i \cdot \nabla)\boldsymbol{u}_i + e\nabla\phi = 0, \tag{18}$$

which must be supplemented with upstream boundary conditions at $z = 0$, n_{i0} and $\boldsymbol{u}_{i0}$.

These hyperbolic equations can be solved numerically for a given ϕ, with equation (18) providing $\boldsymbol{u}_i$ by direct propagation of ion trajectories with the method of characteristics [27]. Once $\boldsymbol{u}_i$ is known, discretization of equation (17) in the plume domain gives n_i.

2.3. Self-consistent electric potential determination

The electron and ion models defined above can be used to compute the zeroth-order n_e, $\boldsymbol{u}_e$, and n_i, $\boldsymbol{u}_i$ at any point (z, r) of the plume, given an electric potential map $\phi(z, r)$ and a set of compatible boundary upstream conditions $\bar{f}^+_{e0}$, n_{i0}, and $\boldsymbol{u}_{i0}$. The quasineutrality assumption and current-free condition in the paraxial limit couple the two species together and allow finding the self-consistent plume solution iteratively, including the electric potential:

$$n_i = n_e; \quad n_i u_{zi} = n_e u_{ze}. \tag{19}$$

The generalization of the second condition to a given non-zero net electric current in the plume is straightforward.

Observe that n_e can be decomposed as $n_e = n_e^+ + n_e^-$, where the $+$ and $-$ signs denote the contributions of $\bar{f}_e^+$ and $\bar{f}_e^-$, respectively. Similarly, $u_{ze} = u_{ze}^+ + u_{ze}^-$. Since $\bar{f}_e^-$ at $z = 0$ is part of the solution, only n_{e0}^+ and u_{ze0}^+ are known *a priori* at the upstream boundary. Indeed, the values of n_{e0}^- and u_{ze0}^- depend on the fraction of *reflected electrons* that

return to the plasma source. Thus, it is not possible, in general, to determine whether the upstream boundary conditions are compatible with equations (19) at $z = 0$ without solving the electron expansion. To overcome this difficulty, only the shape, but not the magnitude, of $\bar{f}_{e0}^{+}$ is prescribed:

$$\bar{f}_{e0}^{+} = n_{e0}^{+}(0)\bar{F}_{e0}^{+} \tag{20}$$

where F_{e0}^{+} is the specified normalized distribution function, and $n_{e0}^{+}(0)$ is the magnitude of $\bar{f}_{e0}^{+}$ to be computed as part of the solution.

Finally, fixing $\phi(0,\ 0) = 0$ at the origin, an iterative solution procedure can then be established as follows: an initial guess of the function $\phi(z, r)$ and the parameter $n_{e0}^{+}(0)$ is produced. The electron and ion models are solved to obtain n_e, u_{ze}, n_i, and u_{zi} at a set of evaluation nodes (z_i, r_i) for $i = 1, \ldots, N$. Equations (19) at those points provide $2N$ error equations to be zeroed. Next, an iterative method is used to generate a new guess of $\phi(z, r)$ and $n_{e0}^{+}(0)$ to lower this error, and the procedure is repeated until convergence with a prescribed tolerance is achieved. Upon completion, the solution method yields the self-consistent $\phi(z, r)$ and $n_{e0}^{+}(0)$.

3. Radially-parabolic potential and semi-Maxwellian electrons

Applying a constraint on the radial shape of the electric potential allows reducing the electron integrals of J_r and β_r in equations (5) and (6) to closed forms, simplifying the solution process. In this section, solutions with a radially-parabolic potential are sought,

$$\phi(h, r) = -\frac{T_e^* h_0^2}{e h^4} r^2 + \phi_z(h), \tag{21}$$

where $h(z)$ is a monotonically-increasing function that represents the (unknown) characteristic radius of the plasma plume at each axial position z with $h(0) = h_0$, and $h(z)$ has been used to replace z as the independent variable of the problem. In expression (21), $\phi_z(h)$, with $\phi_z(h_0) = 0$, is the value of the unknown electric potential along the plume axis, and T_e^* is a characteristic energy constant. The radial electron density profile of equation (21) results in a Gaussian density profile $n_e \propto \exp(-r^2/h_0^2)$ in the limit of isothermal electrons with temperature T_e^*. Such a radial potential profile is therefore a reasonable model of the far-region plasma plume and agrees well with experimental measurements of many GITs and HETs [27]. Observe that the non-separability of ϕ stems from the first term in the right-hand side of equation (21) only, and that the potential for each h is that of a harmonic oscillator in r and θ.

For this electric potential, the corresponding expression for J_r from equation (5) is

$$\frac{J_r}{\pi} = \sqrt{\frac{m_e}{2T_e^*}}\frac{h^2}{h_0}\left[\frac{1}{2m_e}\left(p_r^2 + \frac{p_\theta^2}{r^2}\right) + \frac{T_e^* h_0^2}{h^4} r^2\right] - |p_\theta|. \tag{22}$$

For brevity, the *perpendicular momentum* is defined as

$$p_\perp = \frac{J_r}{\pi} + |p_\theta|, \tag{23}$$

and a characteristic velocity and momentum are defined,

$$c^* = \sqrt{\frac{T_e^*}{m_e}}; \quad p^* = m_e h_0 c^*. \tag{24}$$

Then, β_r from equation (6) is related to r through:

$$\cos(2\pi\beta_r) = \frac{p_\perp - \sqrt{2}p^* r^2/h^2}{\sqrt{p_\perp^2 - p_\theta^2}}, \tag{25}$$

and the extreme values of r in a radial electron orbit, r_+ and r_-, are given by

$$\frac{r_\pm^2}{h^2} = \frac{p_\perp \pm \sqrt{p_\perp^2 - p_\theta^2}}{\sqrt{2}p^*}. \tag{26}$$

Equation (14), which defines the axial turning-point manifold, becomes:

$$\frac{1}{2}m_e v_z^2 = E - U_{\text{eff}}(h, p_\perp) = 0, \tag{27}$$

where:

$$U_{\text{eff}}(h, p_\perp) = -e\phi_z(h) + \sqrt{2}T_e^*\frac{h_0^2}{h^2}\frac{p_\perp}{p^*}, \tag{28}$$

is the *effective potential* of the axial electron motion, which depends on J_r and p_θ only through $p_\perp$. Inverting equation (27) the maximum value of $p_\perp$ for each E and h is given by:

$$p_{\perp M}(h, E) = p^*\frac{h^2}{h_0^2}\frac{E + e\phi_z(h)}{\sqrt{2}T_e^*}. \tag{29}$$

The shape of the turning-point manifold is illustrated in figure 2 for an example function $\phi_z(h)$. Locating the extrema of either U_{eff} or $p_{\perp M}$ along h helps to determine the connectivity of each point of electron phase space with the upstream and downstream boundary conditions efficiently, and thus dividing it into regions of types 1 to 4, as defined in section 2.

As seen in figure 2(a), the effective potential U_{eff} approaches the asymptotic value $-e\phi_\infty$ as $h \to \infty$, where $\phi_\infty = \phi_z(\infty) < 0$. For each $p_\perp$, electrons can only exist in the part of the diagram above the corresponding curve. Free electrons occupy the region of energies larger than the global maximum of the corresponding line. Reflected electrons exist for those $p_\perp$for which the initial value of the curve is lower than the asymptotic value. Finally, doubly-trapped electrons exist only when the curve has a minimum inside the plume domain.

The intersection of the axial turning-point manifold, equation (27), with a $h =$ const plane, is a straight line $s(h)$ for each value of h, as can be observed in figure 2(b), illustrating that the manifold is a ruled surface. This feature enables a simple analysis of the geometry of the electron phase space, as discussed in section 3.1. As h is increased from h_0 to ∞, the slope of the straight line $s(h)$ decreases and its intersection with the energy axis moves up, transforming continuously from the diagonal line $s(h_0)$ to $s(\infty)$. These two limit lines divide the electron phase space into four sectors A, B, C and D. Free electrons can only exist in sector A, above both $s(h_0)$ and $s(\infty)$, whereas reflected electrons can only exist in sectors A or B, above $s(h_0)$. Empty regions can only

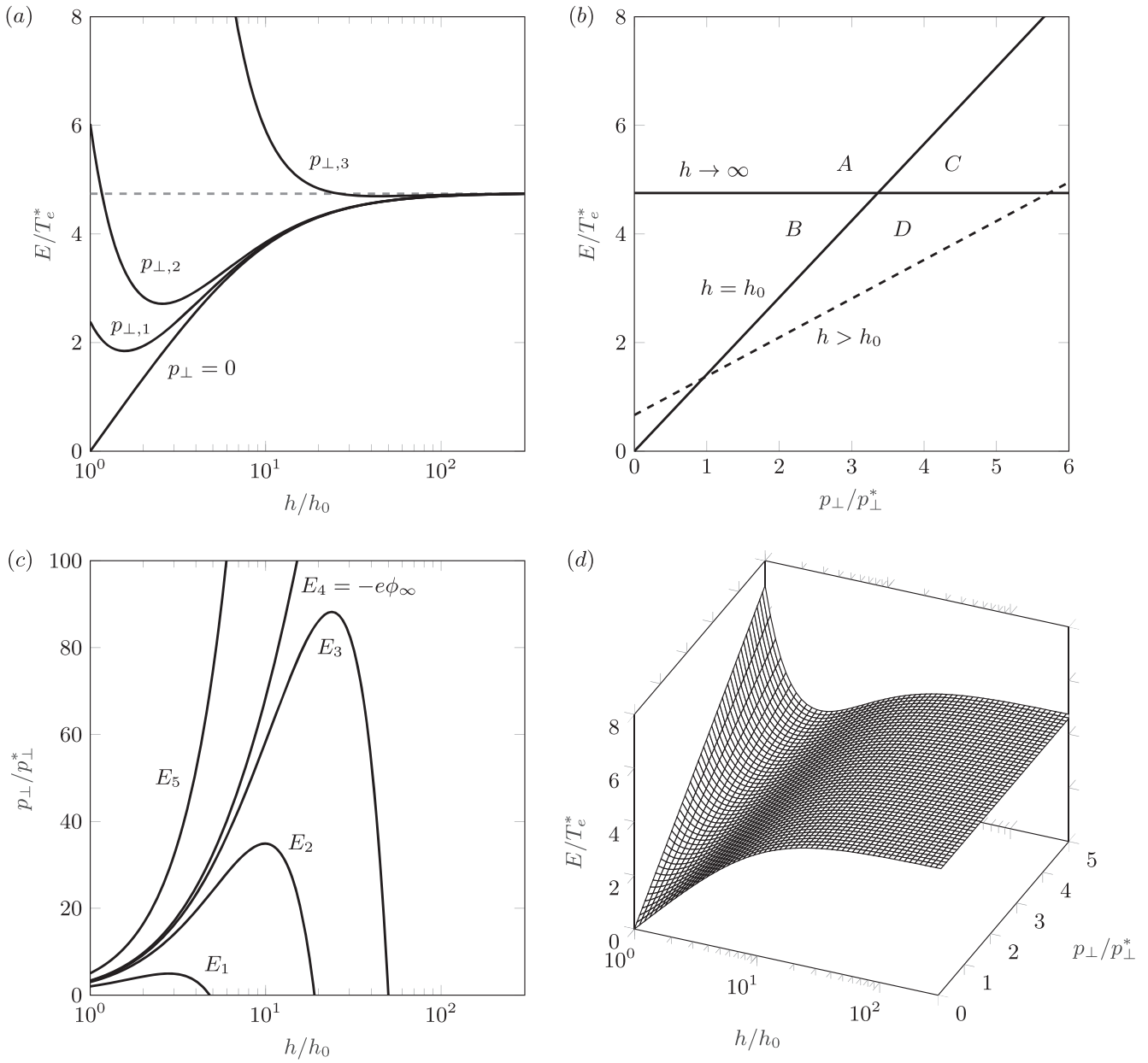

Figure 2. Electron axial turning-point manifold for the radially-parabolic electric potential of equation (21). (a) The effective potential $U_{\rm eff}$ versus h for various values of $p_\perp$, for $0 < p_{\perp 1} < p_{\perp 2} < p_{\perp 3}$. The asymptotic value $-e\phi_\infty/T_{\rm e}^*$ is shown as a dashed line. (b) The effective potential $U_{\rm eff}$ versus $p_\perp$ for $h = h_0$ (the upstream boundary condition), $h = \infty$ (far downstream), and an intermediate value of h (dashed line). (c) The maximum $p_{\perp M}$ versus h for several values of E, for $E1 < E_2 < E_3 < E_4 = -e\phi_\infty < E_5$. (d) Three-dimensional view of the turning-point surface in the E, $p_\perp$, h space. For the purpose of illustration, the solution $\phi_z(h)$ for the case $\alpha = 1$, $\chi = 0.02$, $\mu \to \infty$ (defined in equation (34)) has been chosen.

form in sectors A or C, above $s(\infty)$. Finally, doubly-trapped electrons may exist everywhere, and they are the only type of electrons that can exist in sector D, below both $s(h_0)$ and $s(\infty)$.

In figure 2(c), the allowed region for each energy E is upper bounded by the corresponding curved line. All energies $E < -e\phi_\infty$ (e.g. E_1, E_2, and E_3 in the figure) result in lines that intersect the horizontal axis, so there are no free electrons with those energies; reflected electrons exist for $p_\perp$below the value of the curve at $h = h_0$, whereas doubly-trapped electrons are present if the curve has a maximum inside the plume domain. The lines for energies $E > -e\phi_\infty$ (like E_5) diverge downstream, and free electrons occupy all $p_\perp$below the global minimum of the curve. A three-dimensional view of the axial turning-point surface is shown in figure 2(d).

To further simplify the model, and as a case of practical interest, a semi-Maxwellian population is assumed upstream,

$$\bar{f}_{\rm e0}^{+} = f_{\rm e}^{M} = 2n_{\rm e0}^{+}(0)\left(\frac{m_{\rm e}}{2\pi T_{\rm e}^*}\right)^{3/2} \exp\left(-\frac{E}{T_{\rm e}^*}\right), \qquad (30)$$

where the previously-introduced dimensioning constant T_e^* is the reference temperature. It should be observed that, as $\bar{f}_{e0}^- \neq \bar{f}_{e0}^+$ in general, the upstream electron temperature T_{e0} does not coincide with T_e^*. Only in the limit where the free electron population is negligible (and all electrons at the source are reflected electrons) does $T_{e0} \to T_e^*$.

In order to fully determine the electron distribution function in the doubly-trapped regions, it is assumed that they are populated by a fraction of the same distribution function,

$$\bar{f}_{e(4)}^+ = \bar{f}_{e(4)}^- = \alpha f_e^M, \tag{31}$$

where α is a chosen filling factor between 0 and 1.

The moment integrals of the electron species and subpopulations for the radially-parabolic electric potential case, and in particular for the semi-Maxwellian distribution of above, are reduced to compact expressions in the second part of the appendix.

With regards to ions, their continuity equation (17) under the paraxiallity assumption becomes

$$1 = \frac{n_i(h,\,0)}{n_{i0}(0)} \frac{u_{zi}(h,\,0)}{u_{zi0}(0)} \frac{h^2}{h_0^2}. \tag{32}$$

Lastly, their momentum equation (18) at the plume axis can be integrated into the conservation of ion mechanical energy

$$0 = \frac{1}{2} m_i [u_{zi}^2(h,\,0) - u_{zi0}^2(0)] + e\phi_z(h). \tag{33}$$

The iteration procedure used to determine the self-consistent $\phi_z(h)$ and $n_{e0}^+(0)$ is simplified by taking the N evaluation nodes at the axis of the plume as shown in figure 1, the last of which is taken at $h = \infty$ (i.e. for $z = \infty$). This yields $N - 1$ quasineutrality error equations for the nodes with $h < \infty$, plus a single independent equation for the current-free condition, for a total of N equations. After fixing $\phi_z(h_0) = 0$, there are $N - 1$ unknowns in the discretized $\phi_z(h)$, plus one unknown in $n_{e0}^+(0)$, for a total of N unknowns. Therefore, the iteration scheme is well-posed. This approach has been implemented into the open source numerical code named AKILES2D [49], after 'Advanced Kinetic Iterative pLasma Expansion Solver 2D.'

The resulting model can be normalized with m_e, e, T_e^*, h_0 and $n_{i0}(0)$. The dimensionless plasma response is a function of the filling factor α, the dimensionless velocity parameter χ, and the square root of the ion-electron mass ratio μ:

$$\alpha; \quad \chi = \frac{u_{i0}(0)}{c^*}; \quad \mu = \sqrt{\frac{m_i}{m_e}}. \tag{34}$$

The parameter χ equals the ratio of ion current to thermal electron flux, based on T_e^* rather than $T_{e0}(0)$. The initial ion Mach number at the axis is related to χ and μ through

$$M_{i0}(0) = \frac{u_{i0}(0)}{\sqrt{T_{e0}(0)/m_i}} = \mu\chi \frac{T_e^*}{T_{e0}(0)}, \tag{35}$$

so $\chi \simeq M_{i0}(0)/\mu$, with the factor $T_e^*/T_{e0}(0) \sim 1$ to be computed as part of the solution. Since $u_{e0}(0) = u_{i0}(0)$ from equation (19), χ can also be regarded as the electron Mach number, and $\chi \ll 1$ is expected in actual plasma thruster plumes. Indeed, the range of χ from 0.002 to 0.2 amply covers all current and foreseen electric propulsion applications.

Observe that the dependency on μ is only introduced into the problem through m_i in equation (33). For a fixed value of χ and taking μ, $M_{i0}(0) \to \infty$, the ion velocity remains constant in the expansion, $u_{zi} = u_{zi0}$, and the dependency on μ (or $M_{i0}(0)$) disappears from the problem. This is referred to as the *hypersonic limit* [27]. Thus, the plasma response in hypersonic electric propulsion plumes depends dominantly on α and χ, while the dependency on μ is secondary.

As a final comment, while the model formulated here has been left as a function of the characteristic plume radius at each actual position, $h(z)$, observe that it is possible to determine the dependency of h on z by integrating the full ion model of section 2.2 without using the paraxial approximation of equation (32). Several approximated methods exist to determine the evolution of the characteristic plume radius in hypersonic plasma plumes [27].

3.1. Geometry of the electron phase space

As explained above, the turning-point manifold of equation (27) is a ruled surface. The expression of the parametric family of straight lines $s(h)$ is given by

$$s(h)\colon E + e\phi_z(h) - \sqrt{2}\,T_e^* \frac{h_0^2}{h^2} \frac{p_\perp}{p^*} = 0. \tag{36}$$

In particular, $s(h)$ for $h = h_0$ (i.e. at $z = 0$) and for $h \to \infty$:

$$s(h_0) : E - \sqrt{2}\,T_e^* \frac{h_0^2}{h^2} \frac{p_\perp}{p^*} = 0, \tag{37}$$

$$s(\infty) : E + e\phi_\infty = 0. \tag{38}$$

For later reference, the line $s(h)$ in velocity space at $r = 0$ is simply $v_z = 0$, and $s(h_0)$, $s(\infty)$ are the following curve and circle, respectively:

$$s(h_0) : v_z^2 - v_r^2\left(\frac{h^2}{h_0^2} - 1\right) - \frac{2e}{m_e}\phi_z(h) = 0, \tag{39}$$

$$s(\infty) : v_z^2 + v_r^2 - \frac{2e}{m_e}(\phi_z(h) - \phi_\infty) = 0. \tag{40}$$

In order to determine the phase space domain of the four electron subpopulations described in section 2.1 for a particular value $h = h_1$ with $h_0 \leqslant h_1 \leqslant \infty$, it is necessary to take into account the shape of the whole family $s(h)$ (i.e. for all values of h, not just h_1).

There is, however, one particular situation in which free electrons are determined solely by $s(h_0)$ and $s(\infty)$. Observe that sector A of figure 2(b) is the maximum possible extension of free electrons for a given value of ϕ_∞. If the line $s(h)$ never enters sector A, then this sector *is* the free electron region. According to equations (36)–(38), this condition is met when $\phi_z(h)$ satisfies

$$\frac{\phi_z(h)}{\phi_\infty} \leqslant 1 - \frac{h_0^2}{h^2} \tag{41}$$

for all values of h. Then, the free electron population depends only on the initial plume conditions and the value of ϕ_∞, and

the quasineutrality and current-free conditions at $h = h_0$ suffice to determine ϕ_∞ and $n_{e0}^+(0)/n_{i0}(0)$ as a function of χ. In particular, for the semi-Maxwellian population at the upstream boundary of equation (30), the two expressions of equation (19) yield:

$$\frac{n_{i0}(0)}{n_{e0}^+(0)} = 1 + \operatorname{erf}\sqrt{\frac{-e\phi_\infty}{T_e^*}} - \sqrt{\frac{-2e\phi_\infty}{\pi T_e^*}}\exp\left(\frac{e\phi_\infty}{T_e^*}\right), \\ = \frac{1}{\chi}\sqrt{\frac{2}{\pi}}\left(1 - \frac{e\phi_\infty}{T_e^*}\right)\exp\left(\frac{e\phi_\infty}{T_e^*}\right). \quad (42)$$

The value of $|\phi_\infty|$ obtained from equation (42) can be regarded as the maximum potential fall along the plume that may develop for a given electron current, i.e. for a fixed value of χ, which occurs if and only if no intermediate U_{eff} barriers limit the free electron region.

If, in addition, the intersection between $s(h)$ and $s(\infty)$ always moves rightward in the $(p_\perp, E)$ plane as h increases, then there are no doubly-trapped electrons above $s(\infty)$. Hence, sector C can only have empty regions. This occurs when the decrease rate of $\phi_z(h)$ satisfies the lower bound

$$\frac{d\phi_z}{dh} \geqslant 2\frac{\phi_\infty - \phi_z(h)}{h}, \quad (43)$$

for all h. Observe that this condition is a more demanding, differential version of equation (41).

Finally and likewise, if the intersection between $s(h)$ and $s(h_0)$ always moves rightward in the $p_\perp$, E plane as h increases, then sector B can only have reflected electrons. The necessary condition is the upper bound

$$\frac{d\phi_z}{dh} \leqslant \frac{2\phi_z(h)h_0^2}{h^3 - hh_0^2}. \quad (44)$$

If equations (43) and (44) are both satisfied, then each of the four sectors of phase space contains only one type of electrons, making the computation of moments of $\bar{f}_e$ particularly simple. Note however that the fulfillment of these conditions is not known *a priori*, and therefore they cannot be used in general to simplify the electron model.

4. Results

The paraxial plasma plume model with the radially-parabolic electric potential and semi-Maxwellian source electrons is integrated next to investigate the plasma expansion into vacuum. The analysis focuses first on the case of completely-filled doubly-trapped electron regions ($\alpha = 1$) in section 4.1. The study of other regimes is approached in section 4.2.

4.1. Filled doubly-trapped electron regions

The converged solution for $\alpha = 1$ of the electric potential at the plume axis, $\phi_z(h)$, is shown in figure 3(a) for several values of χ, μ; the 2D electric potential profile for $\chi = 0.02$, $\mu = \infty$ is illustrated in figure 3(b). The electric potential $\phi_z(h)$ decreases monotonically downstream from 0 to an asymptotic value ϕ_∞; most of the potential fall occurs early in the expansion. As can be observed, increasing χ results in a faster approach to the asymptote. A finite value of μ does not affect the expansion substantially unless the initial ion Mach number $M_{i0}(h_0)$ is sufficiently low: for xenon ions ($\mu = 489$) and $\chi = 0.002$, this is $M_{i0}(h_0) \simeq 1$, and the potential approaches ϕ_∞ faster in this case than in the

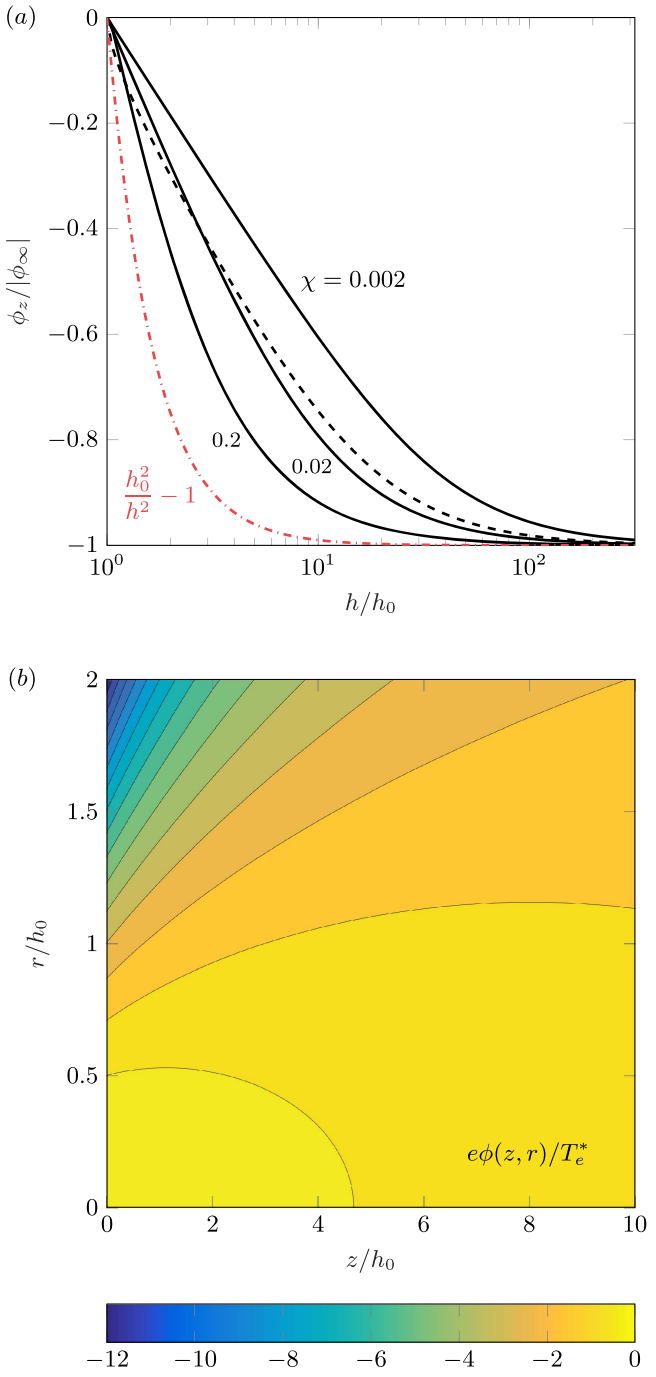

Figure 3. (a) Electric potential $\phi_z(h)/\phi_\infty$ along the plume axis for $\alpha = 1$, $\mu \to \infty$, $\chi = 0.002$, 0.02, and 0.2 (solid black lines). The dashed line has $\alpha = 1$, $\mu = 4.89 \times 10^2$ (corresponding to Xe) and $\chi = 0.002$ (i.e. initial ion Mach number $M_{i0}(0) \simeq 1$). The limit curve of equation (41) is shown as a red dash-dot line. (b) Two-dimensional plot of the electric potential $\phi(z, r)$ for $\alpha = 1$, $\mu \to \infty$, $\chi = 0.02$, and $h(z) = 1 + 0.15z$. Thin lines are isopotential lines.

hypersonic limit. In contrast, for xenon ions, the curves for $\chi = 0.02$ ($M_{i0}(h_0) \simeq 10$) and $\chi = 0.2$ ($M_{i0}(h_0) \simeq 100$) visually coincide with the corresponding hypersonic limits.

The value of ϕ_∞ itself is plotted as a function of χ in figure 4(a). As χ is increased, there is a larger free ion and electron current, and consequently, $e\phi_\infty/T_e^*$ becomes less negative to allow more electrons to escape downstream. As discussed in section 3.1, when the condition in equation (41) is satisfied, then $e\phi_\infty/T_e^*$ depends only on the value of χ and can be computed from equations (42). This condition is seen to be met for all χ in the studied range of $10^2 \leqslant \mu < \infty$. Hence, in the cases presented, ϕ_z and the rest of magnitudes shown in figure 4 can be computed *a priori* before solving the full kinetic problem, and become independent from parameters μ and α.

The electron temperature tensor is diagonal to zeroth order in ε (see appendix), with components

$$T_{ze}; \quad T_{\perp e} \equiv T_{re} = T_{\theta e}. \tag{45}$$

The average temperature is defined as $T_e = (2T_{\perp e} + T_{ze})/3$. Figure 4 shows that $n_{e0}^+(0)/n_{i0}(0)$ and the temperature ratios ($T_{ze0}(0)/T_e^*$, $T_{\perp e0}(0)/T_e^*$ and $T_{e0}(0)/T_e^*$) decrease with increasing χ when χ is small. Due to the difference between $\bar{f}_e^+$ and $\bar{f}_e^-$ at $h = h_0$, a small degree of temperature anisotropy already exists at the upstream boundary (not visible at the scale shown in figure 4(c).

The maximum possible value of χ for a semi-Maxwellian upstream population is $\sqrt{2/\pi} \simeq 0.8$, for which all electrons at $h = h_0$ are free electrons and no reflected electrons exist (i.e. $n_{e0}^- = 0$). For this maximum value of χ, the electron population at $h = h_0$ is just the semi-Maxwellian $\bar{f}_{e0}^+$, and $\phi_z(h) = 0$ for all h. Near this maximum of χ, $T_{\perp e0}(0)/T_e^*$ has non-monotonic behavior with a minimum value. As a consequence, the average temperature $T_{e0}(0)/T_e^*$ also displays a minimum. Clearly, this limit is well outside the expected range in electric propulsion, where $\chi \ll 1$.

For the rest of this section the discussion focuses on the hypersonic limit ($\mu \to \infty$) with $\chi = 0.02$, unless stated otherwise. The evolution of the electron velocity distribution function $\bar{f}_e$ in the $(E, p_\perp)$ plane is presented in the plots on the left of figure 5. The plots on the right provide $\bar{f}_e$ in the v_z, v_r plane at the plume axis ($r = 0$). At $h = h_0$, only free and reflected electron populations exist. As the plasma expands, the fraction of reflected electrons gradually decreases, doubly-trapped electrons gain relevance, and empty regions appear. As the plume characteristic radius h continues to increase, the doubly-trapped population becomes dominant. Finally, far downstream, as $h \to \infty$ and $\phi_z(h) \to \phi_\infty$, the electron density finally drops to zero and the phase space is divided into a forbidden region and an empty region.

The straight lines $s(h_0)$ and $s(\infty)$ from figure 2 and the corresponding transformed curves in velocity variables at the plume axis, equations (39) and (40), are easily identifiable in figure 5. As explained in section 3.1, these two lines play a central role in the geometry of phase space. Figure 6 depicts $\mathrm{d}\phi_z/\mathrm{d}h$ and the two bounds given in equations (43) and (44), showing that both are satisfied everywhere for $\chi = 0.02$ and $\mu = \infty$. As a consequence, sector A in figure 2(b) is the free

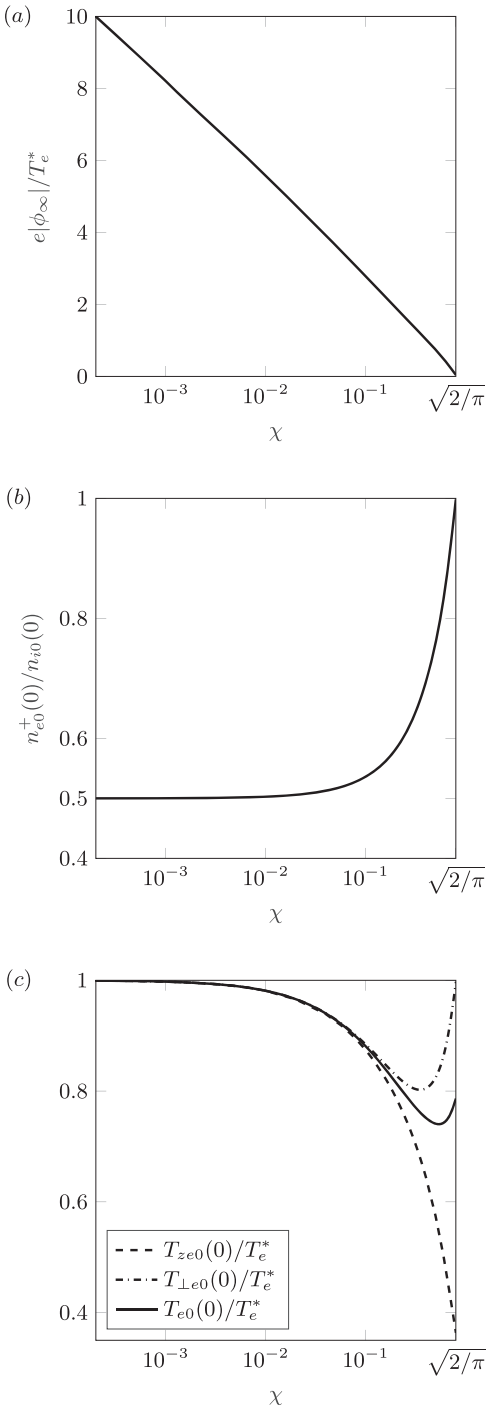

Figure 4. (a) Asymptotic electric potential downstream ϕ_∞. (b) Reflected electron density ratio at the upstream boundary $n_{e0}^+(0)/n_{i0}(0)$. (c) Initial electron temperature ratios $T_{ze0}(0)/T_e^*$ (dashed), $T_{\perp e0}(0)/T_e^*$ (dash-dot), and $T_{e0}(0)/T_e^*$ (solid) as a function of χ for $\alpha = 1$.

electron region, sector B contains reflected electrons, sector C is empty, and sector D contains doubly-trapped electrons.

From equation (32) and the quasineutrality assumption, the electron density along the axis in the hypersonic limit is given by

$$\frac{n_e(h, 0)}{n_{i0}(0)} = \frac{h_0^2}{h^2}, \tag{46}$$

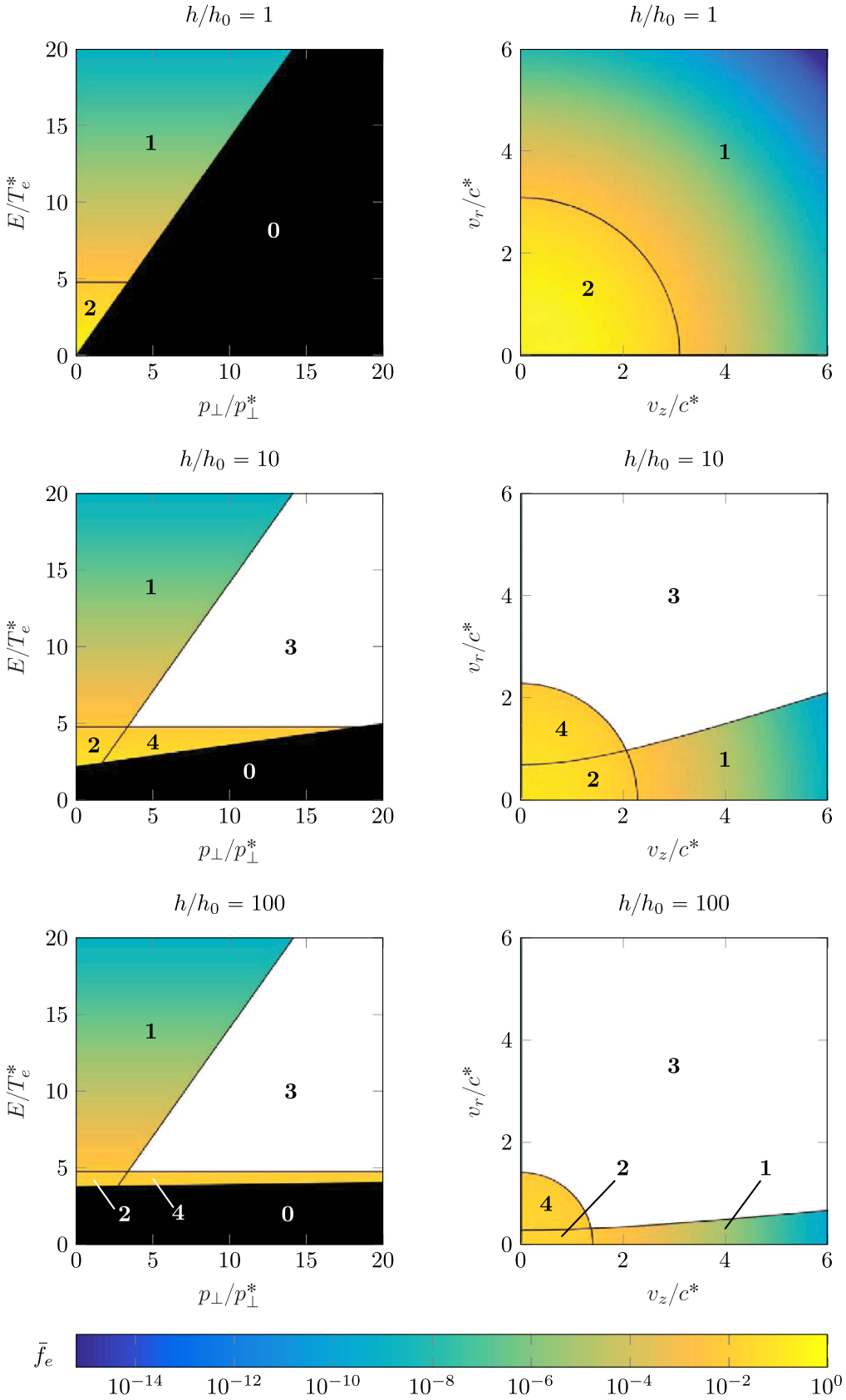

Figure 5. Electron velocity distribution function $\bar{f}_e$ at different values of h, for $\chi = 0.02$, $\mu \to \infty$ and $\alpha = 1$, arbitrary units. Plots on the left show the $(E, p_\perp)$ plane; those on the right the (v_z, v_r) plane at the plume axis ($r = 0$). The color map shows the magnitude of $\bar{f}_e^+$. The different regions of phase space are labeled according to the enumeration of section 2.1: 1, free electrons; 2, reflected electrons; 3, empty regions; 4, doubly-trapped regions.

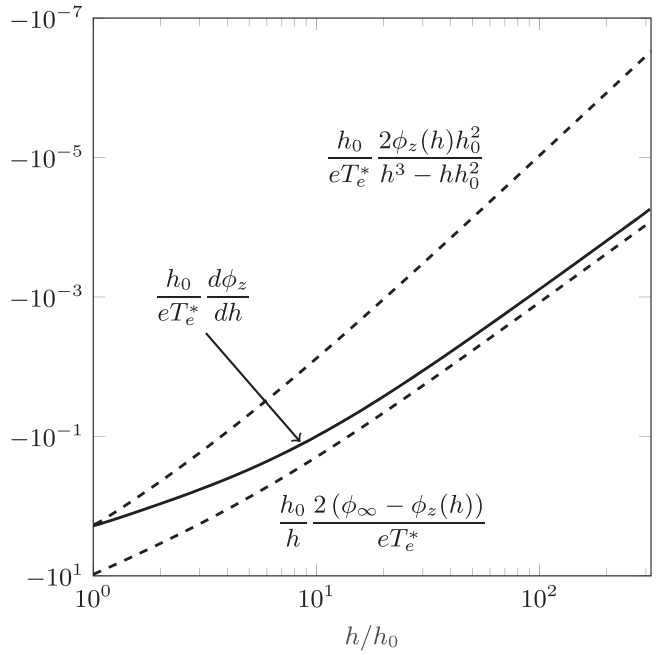

Figure 6. Derivative $\mathrm{d}\phi_z/\mathrm{d}h$ along the plume, and the bounds of equations (43) and (44), for $\chi = 0.02$, $\mu \to \infty$, and $\alpha = 1$.

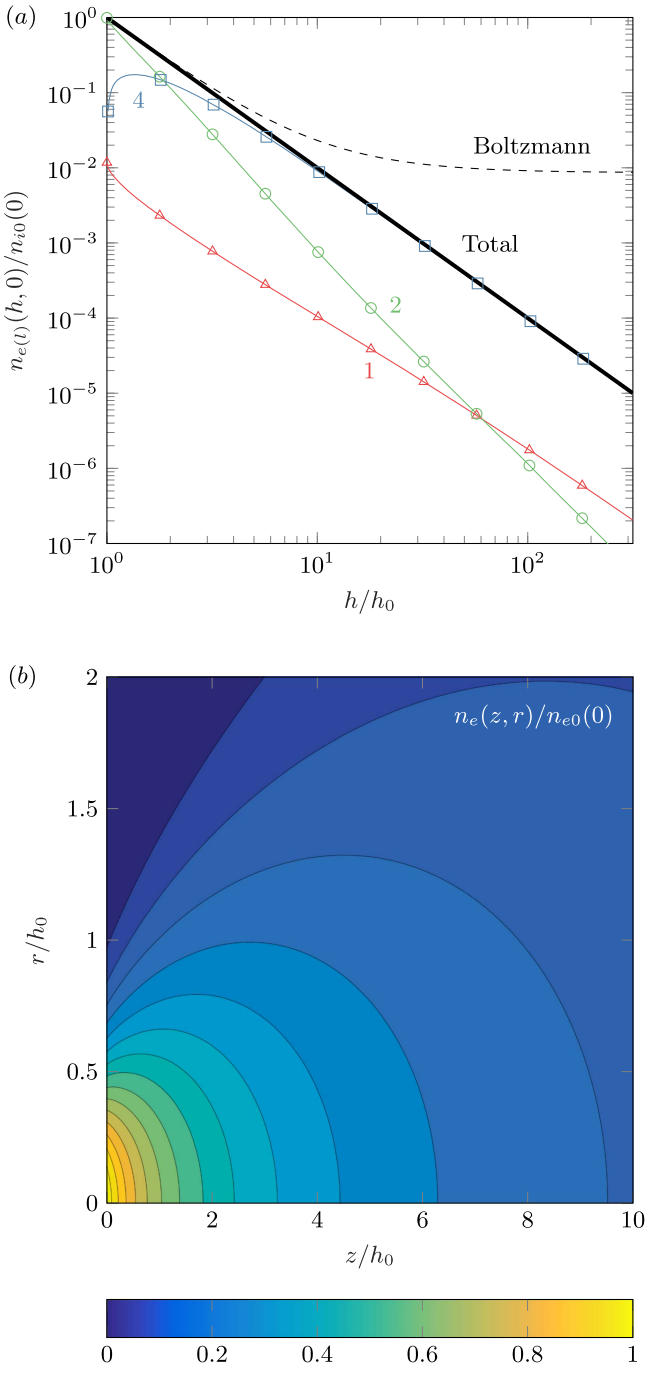

Figure 7. (a) Density $n_e(l)$ of each electron subpopulation 'l' and the whole electron species ('total') at the plume axis for $\chi = 0.02$, $\mu \to \infty$ and $\alpha = 1$. The thin lines represent the densities of free electrons (red triangles), reflected electrons (green circles), and doubly-trapped electrons (blue squares). The thick black line represents the density of the global electron population. The dashed line shows Boltzmann's relation for an isothermal electron species with $T_e = T_e^*$ for comparison. (b) Two-dimensional plot of the total electron density for $\chi = 0.02$, $\mu \to \infty$, $\alpha = 1$. Thin solid lines are contour lines.

This is plotted, together with the density of each electron subpopulation at the plume axis, in figure 7(a). The same conclusions on the dominance of each subpopulation are reached as for figure 5: initially, reflected electrons dominate, but soon doubly-trapped electrons become the majority. Boltzmann's relation for density, $n_e \propto \exp(e\phi_z/T_{e0}(0))$, which would apply for an isothermal expansion, is also plotted for comparison. As can be observed, Boltzmann's relation is only a valid approximation in the first part of the expansion; downstream, density drops at a faster rate, revealing that electron cooling is taking place in that part of the plume. The lower χ is, the larger the region where the (isothermal) Boltzmann's relation adequately describes the expansion. Indeed, Boltzmann's relation is strictly valid only in the singular limit $\chi = 0$, where all electrons are confined and the free electron current is zero. A 2D view of the electron density is shown in figure 7(b). The radial density profile is nearly Gaussian, and the initial radius $r \simeq 1.73h_0$ defines the plasma tube that contains 95% of the plume mass flow.

The axial and perpendicular temperatures T_{ze} and $T_{\perp e} = T_{re}$, $T_{\theta e}$ for each electron subpopulation and for the whole electron species are plotted in figure 8. The average temperature T_e is also shown. For the electron species as a whole, both T_{ze} and $T_{\perp e}$ are nearly constant initially, and then decrease monotonically in the direction of the expansion. This is caused by the partial emptying of the electron distribution function $\bar{f}_e$ as the plasma expands due to (i) the formation of empty regions (type 3 in section 2.1), and (ii) the absence of backward-traveling electrons in free electron regions where $\bar{f}^-_{e(1)} = 0$.

The axial evolution of the electron temperature components is seen to depend strongly on the parameter χ; a lower value of χ results in fewer free electrons, a larger potential fall $|\phi_\infty|$, and smaller empty regions. Consequently, the electron expansion is nearly-isothermal in a larger part of the plume. Indeed, as $\chi \to 0$ (i.e. vanishing net ion and electron current in the plume), the expansion approaches Boltzmann's relation limit as mentioned above.

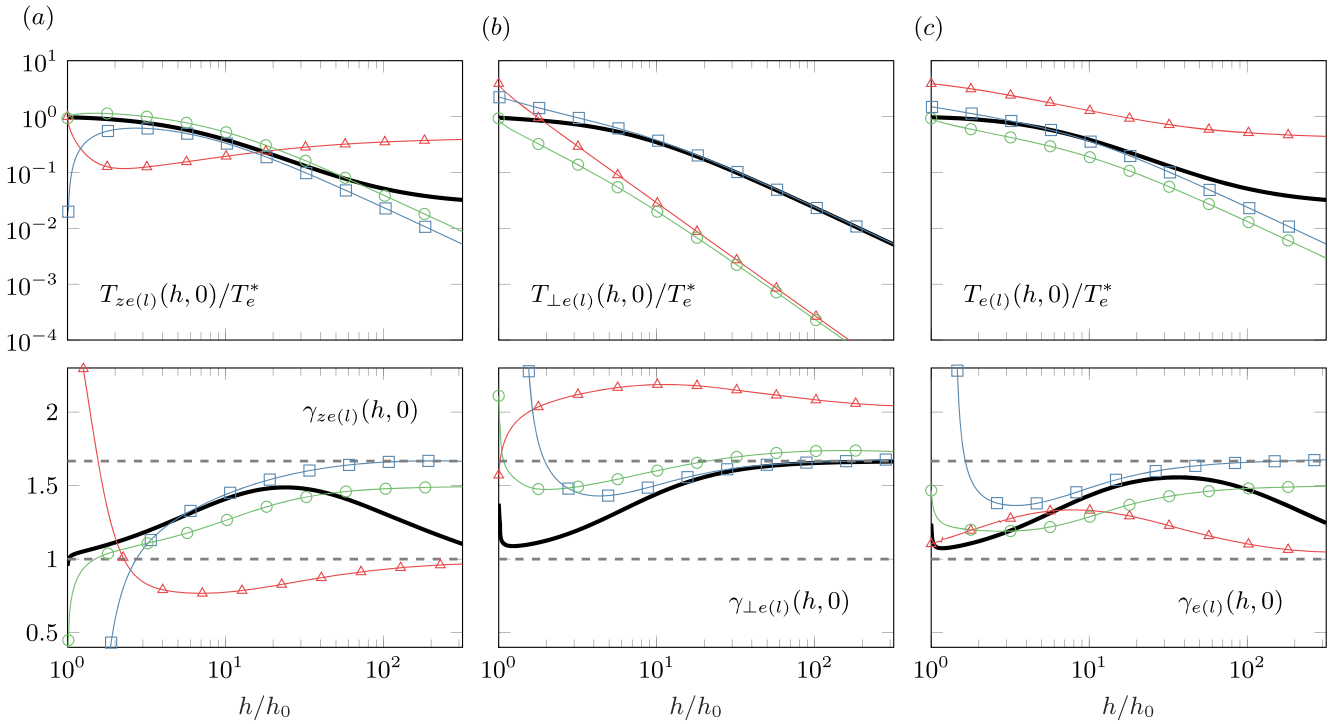

Figure 8. Temperature of each electron subpopulation l and for the whole electron species along the plasma plume axis for $\chi = 0.02$, $\mu \to \infty$ and $\alpha = 1$: (a) $T_{ze(l)}(h,0)/T_e^*$, (b) $T_{\perp e(l)}(h,0)/T_e^*$, and (c) $T_{e(l)}(h,0)/T_e^*$. The thin lines represent the temperature of free electrons (red triangles), reflected electrons (green circles), and doubly-trapped electrons (blue squares). Thick black lines represent the temperatures of the global electron population. The lower plots depict the corresponding *local* cooling exponents $\gamma_{ze(l)}$, $\gamma_{\perp e(l)}$ and $\gamma_{e(l)}$. The dashed lines indicate the limits for an isothermal ($\gamma = 1$) and an adiabatic ($\gamma = 5/3$) behavior.

The two temperature components show, nonetheless, markedly different behaviors downstream: while T_{ze} tends to a small non-zero asymptotic value, $T_{\perp e}$ goes to zero. This can be explained by analyzing the evolution of each subpopulation: in the case of T_{ze}, both the reflected and doubly-trapped electrons have a vanishing contribution as $h \to \infty$, since $T_{ze(2)}$ and $T_{ze(4)}$ go to zero. The free electron $T_{ze(1)}$, by contrast, is non-monotonic, showing a minor increase after an early minimum, and tends to a non-zero asymptotic value downstream. Therefore, it is the free electrons that govern the far-plume behavior of T_{ze}. In the case of $T_{\perp e}$, all subpopulations have $T_{\perp e(l)} \to 0$ downstream, and it is the doubly-trapped electrons $T_{\perp e(4)}$ that dominate nearly everywhere, both due to their larger weight in the electron density, $n_{e(4)}$ and due to their larger perpendicular temperature, $T_{\perp e(4)}$. Finally, although not shown, the components of the electron temperature at a fixed h are nearly constant in the radial direction. This is consistent with the near-Gaussian radial density profile of figure 7(b) that exists at each axial position, which results in a parabolic radial electric potential profile for a radially-isothermal electron species.

The *local* cooling rates for each of the two temperature components and for the average temperature are defined as:

$$\gamma_{ke(l)} = 1 + \frac{\mathrm{d}\ln T_{ke(l)}}{\mathrm{d}\ln n_{e(l)}}, \tag{47}$$

where $k = z, \perp$ for the axial and radial/azimuthal temperatures, and k is left out for the average temperature. The value of these rates along the plume axis is also plotted in figure 8. The initial behavior of these curves is sensitive to the upstream boundary condition $\bar{f}_{e0}^{+}$. The whole-species γ_{ze} is larger where most of the decrease in T_{ze} occurs, and tends to 1 (isothermal limit) far downstream; $\gamma_{\perp e}$, on the other hand, approaches $5/3$ (adiabatic cooling). The cooling exponent for the average temperature, γ_e, results from the combination of these two separate behaviors. Regarding each subpopulation, it is clear that cooling rates outside the range 1–$5/3$ occur, consistent with the behavior of their partial temperatures and densities. In particular, free electrons have $\gamma_{ze(1)} < 1$ and $\gamma_{\perp e(1)} \simeq 2$ in a large part of the plume. This behavior is related to the conversion of radial and azimuthal energy of the free electron subpopulation into axial energy due to the diverging electric potential and the conservation of $p_\perp$.

Figure 9 complements the previous discussion with the (density-specific) axial fluxes of axial, radial and azimuthal thermal energy of each electron subpopulation, as defined in the appendix. Just as in the case of the electron temperature, the heat fluxes of radial and azimuthal thermal energy are equal, $q_{zre} = q_{z\theta e}$. Like any other odd moment in v_z, the heat fluxes of the reflected and doubly-trapped populations are zero. As can be observed, $q_{zze(1)}/n_{e(1)}$ is always positive, and increases slowly downstream after an early minimum. In contrast, q_{zze}/n_e for the whole population decreases. On the other hand, $q_{zre(1)}/n_{e(1)}$ and $q_{z\theta e(1)}/n_{e(1)}$ are negative, indicating that these heat fluxes point towards the plasma source, and go to zero downstream. These behaviors give rise to a

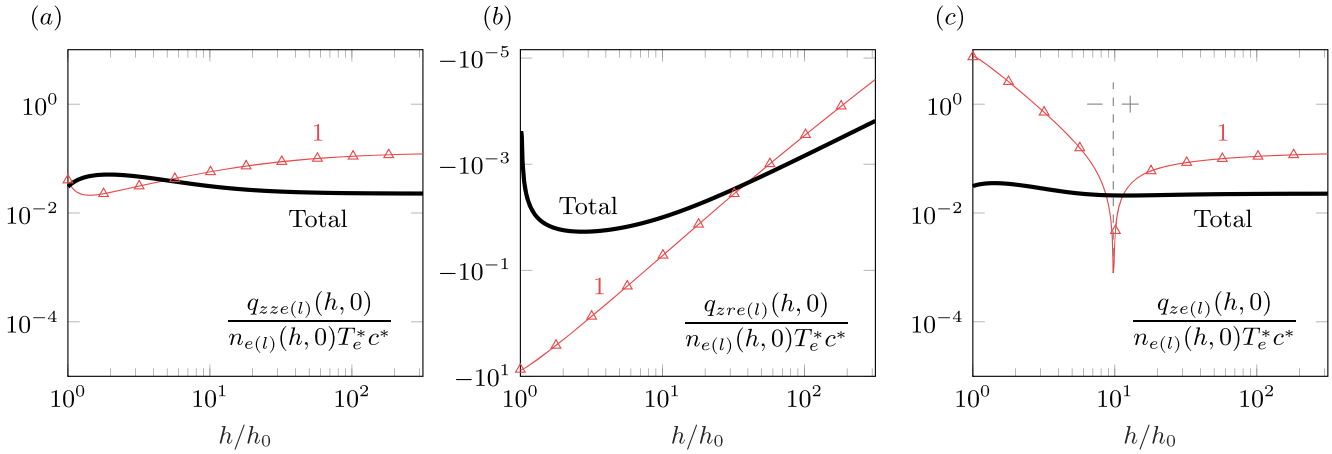

Figure 9. Density-specific kinetic heat fluxes in the axial direction of free electrons ('1') and for the whole electron species ('total') along the plasma plume axis for $\chi = 0.02$, $\mu \to \infty$ and $\alpha = 1$, (a) $q_{zze(l)}(h, 0)/[n_{e(l)}(h, 0)T_e^*c^2]$, (b) $q_{zre(l)}(h, 0)/[n_{e(l)}(h, 0)T_e^*c^2]$, and (c) $q_{ze(l)}(h, 0)/[n_{e(l)}(h, 0)T_e^*c^2]$. The thin lines represent the specific heat flux of free electrons (red triangles) and the thick black lines represent the specific heat flux of the global electron population. In plot (c), the vertical line indicates where $q_{ze(1)}$ changes sign.

$q_{ze(1)}/n_{e(1)}$ that switches sign along the expansion, and a near-constant, positive q_{ze}/n_e. The information about the kinetic heat fluxes can also be used to provide an approximate closure relation for the energy equation of fluid models.

4.2. Partially-filled doubly-trapped electron regions

One of the free parameters of the model of section 3 is α, the filling factor of doubly-trapped regions introduced in equation (31), and assumed $\alpha = 1$ in the previous subsection. When the fraction of doubly-trapped electrons is decreased, the density of the other electron subpopulations must increase to maintain the plasma quasineutrality. Since the number of free electrons is fixed for a given total electric current in the plume, only an increase of reflected electron density can compensate the decrease of doubly-trapped electrons.

To achieve this, the electric potential in the plume must rise to allow more source electrons to travel deeper into the plume before being reflected. The relative change of electric potential is illustrated in figure 10(a) for various values of α. The higher electric potential is apparent in particular in the first part of the expansion. Indeed, the function $\phi_z(h)$ becomes non-monotonic and initially-increasing near the upstream boundary condition, with $\phi_z(h) > \phi_z(h_0)$ in a small region whose size increases as α is decreased. The final potential far downstream, ϕ_∞, is however not affected by α in the range shown.

The relative change of reflected and doubly-trapped electron density is presented in figure 10(b) for $\alpha = 0.7$. As advanced above, more reflected electrons exist to overcome the decrease of doubly-trapped electrons. However, the different slopes of reflected and doubly-trapped electrons in figure 7 mean that the few remaining doubly-trapped electrons eventually become the dominant subpopulation sufficiently downstream.

5. Simple electron cooling model

The results obtained in section 4 can be used to construct closure relations that can inform the fluid electron models of multi-fluid and hybrid codes, replacing Boltzmann's relation and similar laws that are kinetically unjustified for a near-collisionless plasma plume. This can be done with arbitrary level of detail. For example, the average electron temperature can be tabulated against the electron density as a function of χ, μ and α, and the resulting functional dependency $T_e = T_e(n_e; \chi, \mu, \alpha)$ can be used to close the fluid equations at the pressure level. Alternatively, the temperature tensor *components* can be considered; a closure can also be established at the heat flux level using the information of figure 9, or even at higher moments of the distribution function.

It is nonetheless desirable to derive a simple, approximate closure relation that can be readily implemented in existing codes. As most codes already feature a simple polytropic cooling law for electrons, an interesting choice is to establish a polytropic electron cooling model with a constant, averaged cooling rate $\bar{\gamma}_e$ that depends on the plume conditions,

$$\frac{T_e}{T_{e0}(0)} = \left(\frac{n_e}{n_{e0}(0)}\right)^{\bar{\gamma}_e - 1} \tag{48}$$

and respects the electric potential fall $|\phi_\infty|$ of the kinetic model. The total electric potential fall $|\phi_\infty|$ is a key magnitude of the expansion that affects the interaction of the plasma plume with its environment and any nearby objects such as solar arrays. Since $|\phi_\infty|$ is closely linked to the free electron current that escapes downstream, which under the current-free condition must equal the ion current emitted by the thruster, its value is a robust feature of the kinetic model. Since $|\phi_\infty|$ does not show a dependency on μ or α under the parametric range of study, the lumped cooling model is only a function of χ.

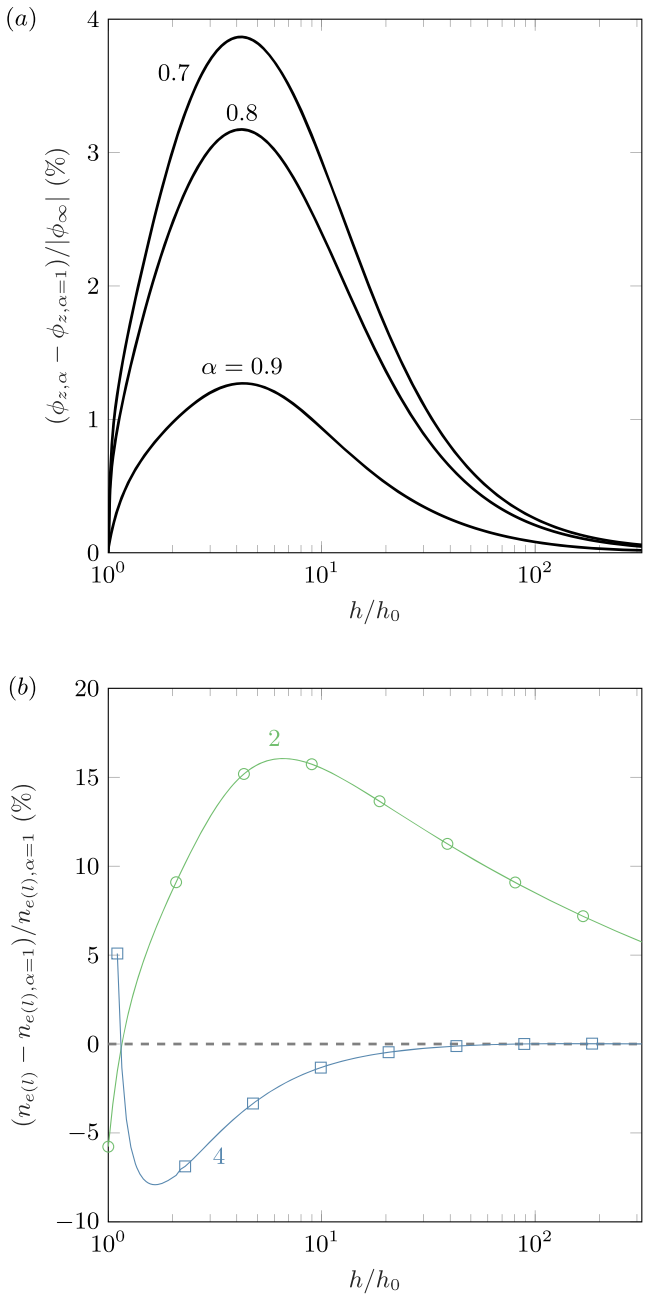

Figure 10. Effect of partially-filled doubly-trapped electron regions for $\chi = 0.02$, $\mu_{\to}\infty$. (a) Relative change of electric potential at the axis $\phi_z(h)$ for $\alpha = 0.9$, 0.8 and 0.7 with respect to the case with $\alpha = 1$. (b) Relative change in reflected (2) and doubly-trapped (4) electron density for $\alpha = 0.7$, with respect to the case with $\alpha = 1$.

For a polytropic electron species, the cooling exponent $\bar{\gamma}_e$ and the asymptotic potential fall ϕ_∞ are related through

$$\bar{\gamma}_e = \frac{|\, e\phi_\infty|}{|\, e\phi_\infty| - T_{e0}(0)}. \tag{49}$$

The value of $\bar{\gamma}_e$ computed from $|\phi_\infty|$ and $T_{e0}(0)$ of the kinetic solution of figure 4 is shown in figure 11. The lumped cooling rate is seen to increase with χ, and becomes infinite at $\chi \simeq 0.4$, for which $e|\,\phi_\infty| \to T_{e0}(0)$, hinting that this approximated closure relation is adequate for modeling the electron expansion only at low values of χ. Moreover, note

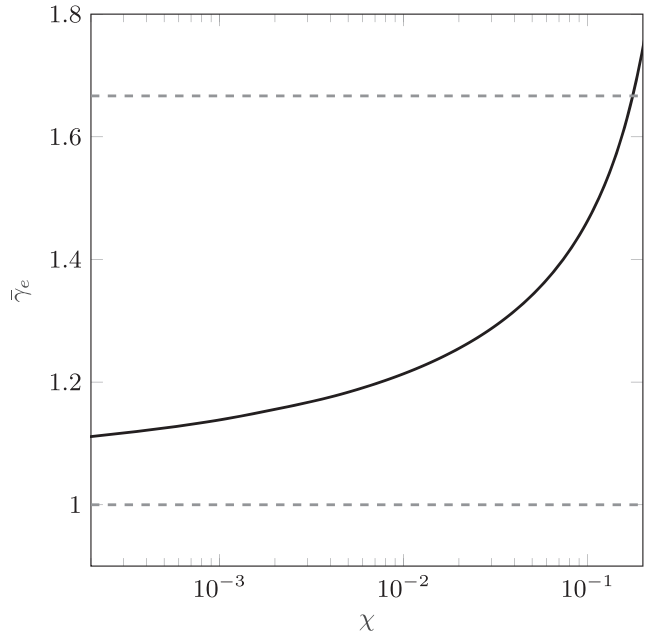

Figure 11. Lumped polytropic model cooling rate $\bar{\gamma}_e$ that results in the same asymptotic potential fall $|\phi_\infty|$ as in the kinetic model, as a function of χ. Dashed lines indicate the isothermal and adiabatic limits.

that this lumped model ignores the local variations of the electron cooling rate and neglects the anisotropy that exists in the plasma plume. For the purpose of comparison, table 1 gathers the reported average polytropic exponent $\bar{\gamma}_e$ in several references. Values for traditional HETs running on xenon cluster around $\chi \simeq 0.02$, $\bar{\gamma}_e \simeq 1.2 - 1.3$.

6. Discussion

There are two aspects of the model that deserve further discussion: firstly, the kinetic model hinges on the expansion being paraxial. The validity of this and other model assumptions is commented on below, in section 6.1. Secondly, the filling of the doubly-trapped electron regions, which are disconnected from both upstream and downstream boundary conditions, cannot be explained from within the present steady-state, collisionless model. This issue is commented on in section 6.2.

6.1. Validity of the model

The validity of the kinetic electron model relies on the adiabatic invariance of J_r. The extent to which J_r is conserved as each electron moves in the axial direction depends on the ratio of the radial electron period, $\tau_r = 1/\dot{\beta}_r$, to the characteristic time τ_{NS} in which the electron experiences changes of the non-separable part of the electric potential. For an electron in the radially-parabolic potential of section 3, equation (8) yields $\tau_r \sim h^2/(h_0 c^*)$, while $\tau_{NS} \sim h^3/(\varepsilon h_0^2 v_z)$, where $\mathrm{d}h/\mathrm{d}z \sim \varepsilon$ and $r \sim h$ have been used. Proper J_r invariance

Table 1. Summary of average polytropic cooling rates $\bar{\gamma}_e$ in plasma thruster plumes reported by experimental and PIC references, for comparison with the lumped model of figure 11. The value of χ for each experimental measurement has been estimated from the available data in those references.

Reference	Reported $\bar{\gamma}_e$	Calculated χ	Comments
[12]	1.30	0.022	BHT-200 measurements. Estimated χ from discharge voltage and T_e.
[17]	1.18	0.021	PPS-1350-ML measurements. Estimated χ from discharge voltage and T_e.
[18]	1.27	0.027	SPT-100-ML measurements. Estimated χ from probe data.
[29]	2.00	0.280	Transient hydrogen plume PIC simulation; planar geometry.

then requires a small value of this time ratio, i.e.

$$\frac{\tau_r}{\tau_{\mathrm{NS}}} \sim \frac{\varepsilon v_z}{c^*}\frac{h_0}{h} \ll 1. \tag{50}$$

From this expression, it is possible to reach three conclusions. Firstly, a small value of ε is necessary, which was an ansatz of the model. Actual plasma thrusters have divergence half angles, defined with the central 95% of the ion current, in the range of 10–15 deg for GITs to 40–50 deg for HETs. Clearly, the paraxiallity criterion is better satisfied by GITs. As explained in section 4, the initial radius of the plasma tube that contains 95% of the current is typically larger than h_0. Secondly, the conservation of J_r and hence the asymptotic expansion in ε is not uniformly valid in velocity space, as it fails for large v_z. This affects, in particular, the high energy tail of the free electron region. Thirdly, J_r invariance improves as h increases, even if the radial electron period increases with h^2.

Apart from these observations, other aspects of the validity of the model as $z \to \infty$ merit their own discussion. As the density decreases, the quasineutrality condition may be called into question. Also, the plasma from the thruster plume eventually merges into the thin ambient plasma, affecting the plasma response in the far downstream region. This may modify, in particular, the amount of electrons that are reflected and doubly-trapped at large values of z. The model also relies on the plasma being collisionless. A small level of collisionality (and instabilities, if any) may not invalidate the results obtained here, but will blur the boundaries between the different phase space regions of the piecewise collisionless solution. Indeed, as discussed in section 6.2, collisions could be particularly relevant as a mechanism for electrons to access doubly-trapped regions. Finally, it is noted that the discontinuity in $\bar{f}_e$ that exists e.g. between free electron regions and doubly-trapped or empty regions leads to an infinite gradient that locally breaks the asymptotic expansion in ε. This phenomenon is expected to give rise to a thin layer around the interface, where $\hat{f}_e$ could be of zeroth order. The solution of these layers has not been addressed in the present work.

6.2. On doubly-trapped electron regions

Section 4.2 provided a preliminary analysis of the effects of partially-populated doubly-trapped regions, assuming that a single parameter α suffices to characterize them. However, the physical mechanisms that may populate these regions are outside of the present model. A qualitative discussion of two of them is presented here.

Firstly, collisionality has been neglected in the model, on the basis that the residence time of ions and electrons in the region of interest of the plume is much shorter than the characteristic collision time in the far-region. Nonetheless, while the free and reflected electron residence time is finite, it is infinite in doubly-trapped regions (in the collisionless limit). This fundamentally affects the time ordering in these regions, and hence the steady-state solution in them must be a collisional one for any non-zero plasma collisionality, even if it is arbitrarily small. This argument supports the choice of a Maxwellian or near-Maxwellian distribution function for these regions. Collisions, hence, could provide a plausible mechanism to populate or depopulate doubly-trapped regions regions over long time scales. Another similar mechanism could be enabled by plasma turbulence.

Secondly, during the transient set-up of the plasma plume, the electric potential changes in time. The mechanical energy of individual electrons is not conserved, and decreases a bit on each reflection at the leading front of the plume expansion. These two effects combined may result in the trapping of electrons into the doubly-trapped regions as they are being formed [45].

7. Conclusions

A collisionless, paraxial plasma plume model was established to investigate the kinetic features of the electron expansion. The model exploits the conservation of mechanical energy and angular momentum about the plume axis, and the adiabaticity of the radial action integral, to integrate the electron Vlasov's equation. Phase space is divided into regions of four different types: free electrons, reflected electrons, empty regions, and doubly-trapped electrons.

The electric potential, the electron velocity distribution function, and its moments up to the heat fluxes were analyzed after prescribing a parabolic shape for the radial electric potential profile and an initially semi-Maxwellian electron population upstream. The expansion depends on three dimensionless parameters, which describe the free ion/electron current, the ion-to-electron mass ratio, and the distribution function in the doubly-trapped regions.

The collisionless cooling of the different electron subpopulations was analyzed in detail. The local cooling exponents were computed, and an approximated, lumped

polytropic model with exponent $\bar{\gamma}_e$ that results in the same total electric potential fall along the plume as in the kinetic plume model was proposed, which is easy to implement in existing fluid and hybrid simulation codes. More precise closure relations that observe the local cooling and the anisotropy of the kinetic solution can be easily derived. Electron cooling is affected by the emergence of empty regions in the electron phase space, as dictated by the effective potential for the electron axial motion, which adds the contributions of the axial change of electric potential and the invariance of the radial action integral. The potential fall $|\phi_\infty|$ is dictated solely by the free ion/electron current in the parametric ranges under study, and hence $|\phi_\infty|$ and $\bar{\gamma}_e$ can be known without solving the whole expansion.

Further investigation must shed light on the filling process of the doubly-trapped regions of phase space. Likewise, other radial electric potential profiles and initial distribution functions than semi-Maxwellian populations should be considered. The effect of background electrons approaching from infinity can be easily included in the model, affecting the previously-empty regions and the free electron regions, as these are both connected to the downstream boundary condition. Finally, the range of validity of the model should be investigated in more detail. A comparison with full-PIC codes and experiments, such as those of [18], will help clarify the range of validity of the model.

Acknowledgments

The authors want to thank Professor Jesús Ramos from the Massachusetts Institute of Technology, and Dr Jaume Navarro, Dr Gonzalo Sánchez-Arriaga, and Dr Pablo Fajardo from Universidad Carlos III de Madrid for many insightful discussions and comments. This work has been supported by ESA project 4000116180/15/NL/PS. The work of Javier Mauriño has been supported by the UK Royal Academy of Engineering's Engineering Leaders Scholarship (ELAA1516/1/87).

Appendix. Computation of moments of the electron distribution function

Following the enumeration of the electron subpopulations given in section 2.1, the *ijk*th moment of electron distribution function $\bar{f}_e$ at a point (z, r) of the plume for the *l*th electron subpopulation is given by:

$$\mathcal{M}_{ijk(l)}(z, r) = \iiint \bar{f}_{e(l)}\, v_z^i v_r^j v_\theta^k \mathrm{d}\boldsymbol{v}, \tag{A1}$$

where the integral extends to all phase space. The total *ijk*th moment for the full electron species is then

$$\mathcal{M}_{ijk} = \mathcal{M}_{ijk(1)} + \mathcal{M}_{ijk(2)} + \mathcal{M}_{ijk(4)}. \tag{A2}$$

Reflected electrons (subpopulation 2) and doubly-trapped electrons (4) do not contribute to odd moments in v_z, which depend only on the free electrons (1). Also, as $\bar{f}_e$ is independent of β_r, it is symmetric in v_r, and for a non-rotating plume, $\bar{f}_e$ is also symmetric in v_θ. Hence, the integral vanishes for odd j or k.

Several derived quantities are commonly defined from the moments of the distribution function and are used in the text. As in equation (A2), a subindex in parenthesis, if present, denotes a single electron subpopulation. A variable without such a subindex refers to the full electron species. Electron densities are

$$n_{e(l)} = \mathcal{M}_{000(l)}. \tag{A3}$$

Axial velocities are defined as:

$$u_{ze(l)} = \frac{\mathcal{M}_{100(l)}}{n_{e(l)}}, \tag{A4}$$

with $u_{ze(2)} = u_{ze(4)} = 0$. Note that $u_{ze(1)} \neq u_{ze}$ as it is weighted with a different density. The temperature tensor is diagonal, with

$$T_{ze(l)} = m_e\left(\frac{\mathcal{M}_{200(l)}}{n_{e(l)}} - u_{ze(l)}^2\right), \tag{A5}$$

$$T_{re(l)} = m_e\frac{\mathcal{M}_{020(l)}}{n_{e(l)}}, \tag{A6}$$

$$T_{\theta e(l)} = m_e\frac{\mathcal{M}_{002(l)}}{n_{e(l)}}, \tag{A7}$$

The average temperature is defined as $T_{e(l)} = (T_{ze(l)} + T_{re(l)} + T_{\theta e(l)})/3$. Observe that $T_{re} = T_{\theta e}$, and the symbol $T_\perp$ is used to denote either of them in the text. Also, note that $n_e T_{ze} \neq \sum n_{e(l)} T_{ze(l)}$ due to the u_{ze}^2 term. Finally, the heat fluxes of axial, radial, and azimuthal thermal energy in the axial direction are:

$$q_{zke(l)} = \frac{m_e}{2}\iiint \bar{f}_{e(l)}\,(v_z - u_z)(v_k - u_k)^2 \mathrm{d}\boldsymbol{v} \tag{A8}$$

where $k = z, r, \theta$, i.e.:

$$q_{zze(l)} = \frac{m_e}{2}\mathcal{M}_{300(l)} - \frac{3}{2}n_{e(l)}u_{ze(l)}T_{ze(l)} - \frac{m_e}{2}n_{e(l)}u_{ze(l)}^3,$$
$$q_{zre(l)} = \frac{m_e}{2}\mathcal{M}_{120(l)} - \frac{3}{2}n_{e(l)}u_{ze(l)}T_{re(l)},$$
$$q_{z\theta e(l)} = \frac{m_e}{2}\mathcal{M}_{102(l)} - \frac{3}{2}n_{e(l)}u_{ze(l)}T_{\theta e(l)},$$

and the total heat flux in the axial direction is $q_{ze} = q_{zze} + q_{zre} + q_{z\theta e}$.

In the case of a radially-parabolic electric potential as in section 3, the even moments of the distribution function in v_r and v_θ for the *l*th electron subpopulation can be computed as the following triple integral in the $(E, p_\perp, p_\theta)$ variables,

$$\mathcal{M}_{ijk(l)}(h, r) = \frac{1}{r^{k+1}}\frac{\sqrt{2^{i+j+3}T_e^*}}{\sqrt{m_e^{i+j+2k+5}}}\frac{h_0}{h^2}\int \mathrm{d}E$$
$$\times \int \mathrm{d}p_\perp [E - U_{\mathrm{eff}}(h, p_\perp)]^{\frac{i-1}{2}} \int \mathrm{d}p_\theta \ldots$$
$$\times \left(\sqrt{2}T_e^*\frac{h_0^2}{h^2}\frac{p_\perp}{p^*} - \frac{T_e^* h_0^2}{h^4}r^2 - \frac{p_\theta^2}{2m_e r^2}\right)^{\frac{j-1}{2}}$$
$$\times p_\theta^k [\bar{f}_{e(l)}^+ + (-1)^i \bar{f}_{e(l)}^-], \tag{A9}$$

which has an avoidable singularity at the plume axis, $r = 0$. In this expression, $h = h(z)$; the integral on p_θ runs from 0 to $r[2\sqrt{2}p^* p_\perp/h^2 - 2(p^*)^2 r^2/h^4]^{1/2}$; the integral on $p_\perp$ from $[(p^*/\sqrt{2})r^2/h^2]$ to $p_{\perp M}$ of equation (29); and the integral on E from $[-e\phi_z(h) + T_e^* h_0^2 r^2/h^4(z)]$ to ∞.

Lastly, if the distribution function at the upstream boundary condition is semi-Maxwellian as in equation (30), the integral simplifies to:

$$\mathcal{M}_{ijk(l)}(h, r) = n_{e0}^{+}(0)(\sqrt{2}c^*)^{i+j+k}\frac{\Gamma\left(\frac{1+j}{2}\right)\Gamma\left(\frac{1+k}{2}\right)}{\pi^{3/2}\Gamma\left(1+\frac{j+k}{2}\right)} \times \exp\left(\frac{e\phi_z(h)}{T_e^*} - \frac{h_0^2}{h^4}r^2\right)G_{ijk(l)}, \tag{A10}$$

with:

$$G_{ijk(l)} = \int_0^\infty \exp(-p_\perp')(p_\perp')^{\frac{j+k}{2}}\mathrm{d}p_\perp' \int_0^\infty \mathcal{P}_{(l)} \times \exp(-E')(E')^{\frac{i-1}{2}}\mathrm{d}E', \tag{A11}$$

where $\mathcal{P}_{(l)} = \mathcal{P}_{(l)}(h, E', p_\perp')$ is equal to 1 for $l = 1, 1 + (-1)^i$ for $l = 2$, $\alpha[1 + (-1)^i]$ for $l = 4$, and 0 otherwise; and

$$E' = \frac{1}{T_e^*}[E + e\phi_z(h)] - \sqrt{2}\frac{h_0^2}{h^2}\frac{p_\perp}{p^*}, \tag{A12}$$

$$p_\perp' = \sqrt{2}\frac{h_0^2}{h^2}\frac{p_\perp}{p^*} - \frac{h_0^2}{h^4}r^2. \tag{A13}$$

The integral in E' in equation (A11) can be reduced in each region of phase space to incomplete gamma functions. Observe that equation (A10) is symmetric in the indices j and k, and therefore the moments in the semi-Maxwellian case satisfy:

$$\mathcal{M}_{ijk} = \mathcal{M}_{ikj}. \tag{A14}$$

ORCID iDs

Mario Merino https://orcid.org/0000-0001-7649-3663
Javier Mauriño https://orcid.org/0000-0002-4941-6053
Eduardo Ahedo https://orcid.org/0000-0003-2148-4553

References

[1] Roy R I S, Gastonis N A and Hastings D E 1996 Ion-thruster plume modeling for backflow contamination *J. Spacecr. Rockets* **33** 525–34
[2] Tverdokhlebova E and Korsun A G 2000 Plasma plume/spacecraft interaction. State of the art in investigation methodology *Spacecr. Propul.* **465** 675
[3] Tajmar M, Gonzalez J and Hilgers A 2001 Modelling of spacecraft-environment interactions on SMART-1 *J. Spacecr. Rockets* **38** 393–9
[4] Goebel D M and Katz I 2008 *Fundamentals of Electric Propulsion: Ion and Hall Thrusters* (New York: Wiley)
[5] Garrett H B and Whittlesey A C 2000 Spacecraft charging, an update *IEEE Trans. Plasma Sci.* **28** 2017–28
[6] Garrett H B and Whittlesey A C 2012 *Guide to Mitigating Spacecraft Charging Effects* (New York: Wiley)
[7] Leboeuf J N, Chen K-R, Donato J M, Geohegan D B, Liu C L, Puretzky A A and Wood R F 1996 Modeling of plume dynamics in laser ablation processes for thin film deposition of materials *Phys. Plasmas* **3** 2203–9
[8] Lieberman M A and Lichtenberg A J 2005 *Principles of Plasma Discharges and Materials Processing* (Hoboken, NJ: Wiley)
[9] Lebedev S V *et al* 2005 Production of radiatively cooled hypersonic plasma jets and links to astrophysical jets *Plasma Phys. Control. Fusion* **47** B465
[10] Myers R M and Manzella D H 1993 Stationary plasma thruster plume characteristics *23rd Int. Electric Propulsion Conf., Seattle, WA* 93–096 IEPC
[11] Gallimore A D 2001 Near- and far-field characterization of stationary plasma thruster plumes *J. Spacecr. Rockets* **38** 361–8
[12] Beal B E, Gallimore A and Hargus W A 2005 Plasma properties downstream of a low-power Hall thruster *Phys. Plasmas* **12** 123503
[13] Foster J E, Patterson M, Pencil E, McEwen H, Diaz E and Van Noord J 2006 Plasma characteristics measured in the plume of a next multi-thruster array *42nd Joint Propulsion Conf.* (https://doi.org/10.2514/6.2006-5181)
[14] Ekholm J M, Hargus W A, Larson C W, Nakles M R, Reed G and Niemela C S 2006 Plume characteristics of the Busek 600 W Hall thruster *Proc. 42nd Joint Propulsion Conf. and Exhibit No. AIAA-2006-4659* (American Institute of Aeronautics and Astronautics) (https://doi.org/10.2514/6.2006-4659)
[15] Nakles M R, Brieda L, Hargus W A Jr, Garrett D R and Randy R L 2007 Experimental and numerical examination of the BHT-200 Hall thruster plume *43rd AIAA/ASME/SAE/ASEE Joint Propulsion Conf. & Exhibit (Washington, DC)* AIAA (https://doi.org/10.2514/6.2007-5305)
[16] Dannenmayer K, Mazouffre S, Merino M and Ahedo E 2012 Hall effect thruster plasma plume characterization with probe measurements and self-similar fluid models *48th AIAA/ASME/SAE/ASEE Joint Propulsion Conf. & Exhibit No. AIAA-2012-4117 (Washington DC)* (https://doi.org/10.2514/6.2012-4117)
[17] Dannenmayer K and Mazouffre S 2013 Electron flow properties in the far-field plume of a Hall thruster *Plasma Sources Sci. Technol.* **22** 035004
[18] Giono G, Gudmundsson J, Ivchenko N, Mazouffre S, Dannenmayer K, Popelier L, Loubere D, Merino M and Olentsenko G 2018 Non-Maxwellian electron energy probability functions in the plume of a SPT-100 Hall thruster *Plasma Sources Sci.Technol.* **27** 015006
[19] Manzella D, Jankovsky R, Elliott F, Mikellides I, Jongeward G and Allen D 2001 Hall thruster plume measurements on-board the Russian express satellites *27th Int. Electric Propulsion Conf. No. IEPC-2001-044 (Pasadena, CA)*
[20] Vicini A, Passaro A and Biagioni L 2004 Hall thruster 3D plume modeling and comparison with SMART-1 flight data *4th Int. Spacecraft Propulsion Conf.*
[21] Hilgers A, Thiébault B, Estublier D, Gengembre E, Del Amo J A G, Capacci M, Roussel J-F, Tajmar M and Forest J 2006 A simple model of the effect of solar array orientation on SMART-1 floating potential *IEEE Trans. Plasma Sci.* **34** 2159–65
[22] Gabdullin F F, Korsun A G and Tverdokhlebova E M 2008 The plasma plume emitted onboard the international space station under the effect of the geomagnetic field *IEEE Trans. Plasma Sci.* **36** 2207–13

[23] Estublier D L 2008 The SMART-1 spacecraft potential investigations *IEEE Trans. Plasma Sci.* **36** 2262–70
[24] Aston G, Kaufman H R and Wilbur P J 1978 Ion beam divergence characteristics of two-grid accelerator systems *AIAA J.* **16** 516–24
[25] Hofer R R and Gallimore A D 2003 Recent results from internal and very-near-field plasma diagnostics of a high specific impulse Hall thruster *28th Int. Electric Propulsion Conf.*
[26] Boyd I D and Dressler R A 2002 Far field modeling of the plasma plume of a Hall thruster *J. Appl. Phys.* **92** 1764
[27] Merino M, Cichocki F and Ahedo E 2015 Collisionless plasma thruster plume expansion model *Plasma Sources Sci. Technol.* **24** 035006
[28] Wang J, Brinza D and Young M 2001 Three-dimensional particle simulation modeling of ion propulsion plasma environment for Deep Space I *J. Spacecr. Rockets* **3** 433–40
[29] Hu Y and Wang J 2015 Electron properties in collisionless mesothermal plasma expansion: fully kinetic simulations *IEEE Trans. Plasma Sci.* **43** 2832–8
[30] Kahnfeld D, Schneider R, Cichocki F, Merino M, Ahedo E, Duras J and Koch N 2017 Comparison of plume simulations of a 2D3V-PIC-MCC and a 3D hybrid-PIC code *35th Int. Electric Propulsion Conf. (Fairview Park, OH)* number IEPC-2017-329 Electric Rocket Propulsion Society
[31] Korsun A G, Tverdokhlebova E M and Gabdullin F F 2004 Simulation of plasma plume-to-spacecraft interaction *Comput. Phys. Commun.* **164** 353–64
[32] Ortega A L, Katz I, Mikellides I G and Goebel D M 2015 Self-consistent model of a high-power Hall thruster plume *IEEE Trans. Plasma Sci.* **43** 2875–86
[33] Oh D Y 1997 Computational modeling of expanding plasma plumes in space using a PIC-DSMC algorithm *25th Int. Electric Propulsion Conf., Cleveland, OH* number IEPC-97-179
[34] VanGilder D B, Font G I and Boyd I D 1999 Hybrid Monte Carlo-particle-in-cell simulation of an ion thruster plume *J. Propul. Power* **15** 530–8
[35] Brieda L, Pierru J, Kafafy R and Wang J 2004 Development of the DRACO code for modeling electric propulsion plume interactions *40th AIAA/ASME/SAE/ASEE Joint Propulsion Conf. and Exhibit* (https://doi.org/10.2514/6.2004-3633)
[36] Wartelski M, Theroude C, Ardura C and Gengembre E 2013 Self-consistent simulations of interactions between spacecraft and plumes of electric thrusters *33th Int. Electric Propulsion Conf.* number IEPC-2013-73
[37] Taccogna F, Pagano D, Scortecci F and Garulli A 2014 Three-dimensional plume simulation of multi-channel thruster configuration *Plasma Sources Sci.Technol.* **23** 065034
[38] Araki S J, Martin R S, Bilyeu D L and Koo J W 2016 SM/MURF: current capabilities and verification as a replacement of AFRL plume simulation tool COLISEUM *52nd AIAA/SAE/ASEE Joint Propulsion Conf.* p 4939
[39] Cichocki F, Domínguez A, Merino M and Ahedo E 2017 Hybrid 3D model for the interaction of plasma thruster plumes with nearby objects *Plasma Sources Sci. Technol.* **26** 125008
[40] Boyd I D and Yim J T 2004 Modeling of the near field plume of a Hall thruster *J. Appl. Phys.* **95** 4575
[41] Passaro A, Vicini A and Biagioni L 2004 3D computation of plasma thruster plumes *40th AIAA/ASME/SAE/ASEE Joint Propulsion Conf. & Exhibit (Washington, DC)* AIAA (https://doi.org/10.2514/6.2004-3632)
[42] Raadu M A 1979 Expansion of a plasma injected from an electrodeless gun along a magnetic field *Plasma Phys.* **21** 331
[43] Martinez-Sanchez M, Navarro-Cavallé J and Ahedo E 2015 Electron cooling and finite potential drop in a magnetized plasma expansion *Phys. Plasmas* **22** 053501
[44] Plaza S C, Navarro J and Ahedo E 2016 Expansion of a collisionless magnetized plasma plume with bi-Maxwellian electrons *52nd AIAA/SAE/ASEE Joint Propulsion Conf.* (https://doi.org/10.2514/6.2016-5035)
[45] Sanchez-Arriaga G, Zhou J, Ahedo E, Martínez-Sánchez M and Ramos J 2017 One-dimensional direct Vlasov simulations of non-stationary plasma expansion in magnetic nozzle *35th Int. Electric Propulsion Conf. No. IEPC-2017-106 (Fairview Park, OH)* (Electric Rocket Propulsion Society)
[46] Martínez-Sánchez M and Ahedo E 2011 Magnetic mirror effects on a collisionless plasma in a convergent geometry *Phys. Plasmas* **18** 033509
[47] Merino M, Mauriño J and Ahedo E 2017 Direct-Vlasov study of electron cooling mechanisms in paraxial, unmagnetized plasma thruster plumes *35th Int. Electric Propulsion Conf. (Fairview Park, OH)* number IEPC-2017-104 Electric Rocket Propulsion Society
[48] Goldstein H, Poole C P and Safko J L 2001 *Classical Mechanics* (Edinburgh: Pearson)
[49] Merino M and Mauriño J 2017 Akiles2d code: advanced kinetic iterative plasma expansion solver 2D doi:10.5281/zenodo.1098432.